Title

Interference-Tolerant Multi-User Radar System

Permalink

https://escholarship.org/uc/item/2s15v5hn

Author

Wu, Yu-Hsiu

Publication Date

2016

Peer reviewed|Thesis/dissertation

Interference-Tolerant Multi-User Radar System

by

Yu-Hsiu Wu

2016

ABSTRACT OF THE DISSERTATION

Interference-Tolerant Multi-User Radar System

by

Yu-Hsiu Wu

Doctor of Philosophy in Electrical Engineering

University of California, Los Angeles, 2016

Professor Mau-Chung Frank Chang, Chair

Autonomous driving of vehicles has been becoming a reality and radar is an indispensable feature of this transportation method. However, there will be interference issues due to the multiple signals transmitted from the radars on the adjacent driving vehicles operating in the same area at the same time. Consequently, radar interference mitigation techniques will be essential in such multi-vehicle environment. In order to accurately detect and localize adjacent vehicles, several radars must be carried on each vehicle. A low-cost and highly-integrated CMOS radar sensor could be the best candidate to fulfill this growing industrial need.

Linear frequency-modulated continuous-wave (FMCW) radar with constant envelope waveform is suitable for low-power/ low-cost CMOS implementation. However, the ghost targets due to other radars and radio interference generate false alarms and lower the probability of detection. Some interference mitigation techniques allocating frequency sub-bands at different time for different users to avoid concurrent frequency band usage have been proposed in the past. However, the number of users must trade off with the available bandwidth so does the range resolution.

This dissertation presents an interference-tolerant radar which can endure multiple signals transmitted from adjacent vehicles for autonomous driving applications. The interference immunity property has been realized by applying a specific code-division multiplexing method,

involved with one-coincidence frequency hopping code, to the continuous-wave radar. A radar prototype has been implemented in 65nm CMOS for operation at 24GHz with 1GHz bandwidth (equivalently with 15cm range resolution). Measurements indicate that the prototype can support up to 22 adjacent vehicles simultaneously by using the optimized Hamming correlation property of the extended hyperbolic congruential code.

The dissertation of Yu-Hsiu Wu is approved.

Songwu Lu

Sudhakar Pamarti

Mau-Chung Frank Chang, Committee Chair

University of California, Los Angeles

2016

Dedicated to my family, especially my mom.

TABLE OF CONTENTS

LIST OF FIGURES

LIST OF TABLES

ACKNOWLEDGEMENTS

First, I would like to thank my advisor Professor Mau-Chung Frank Chang, who accepted me into HSEL and gave me guidance as well as great support, not only for research but also for life. He never limited me and always inspired me opening my vision. I also want to thank my committee members, Professor Itoh, Professor Pamarti, and Professor Lu, for serving on my committee and giving me advices.

Of course, I appreciate all the help from HSEL members. We are like family backing each other up. I feel so lucky to join this lab because of you guys. Finally, it is impossible for me to express my gratitude to my family, especially my mom, who is the mainstay of my life.

VITA

2006   B.S. (Electrical Engineering), National Taiwan University.

2008   M.S. (Electrical Engineering), National Taiwan University.

PUBLICATIONS

Yu-HsiuWu, Yen-Cheng Kuan, M.-C. Frank Chang, "Interference-Tolerant Multi-User Radar System Using One-Coincidence Frequency Hopping Code with 1GHz Bandwidth at 24GHz," *2016 IEEE MTT-S International Microwave Symposium (IMS)*, San Francisco, CA, 2016. (Best Paper Award, 3rd Place Winner)

Chapter 1

Introduction

1.1   Motivation

Autonomous driving of vehicles has been becoming a reality and there are many

sensors equipped on the car shown in Fig. 1.1[1]. GPS locates and directs the vehicle to

the destination. In order to aware of the surroundings, the combination of the stereo

camera, LiDAR, radar, and ultrasound helps mapping nearby features, spotting road

edges and lane markings as well as reading signs, traffic lights, and identifying

pedestrians. Ultrasound provides more accurate mapping of the surroundings at short

range and it has already been used for parking assist for a long time. Finally, computer

collects and calculates the information from multiple sensors and determines which

sensor fits in best in certain condition. For example, stereo camera resembles human

eyes, it is good at defining objects and recognizing the traffic signs. However, it cannot

operate in dark, direct sunlight, and bad weather. LiDAR can help in dark and direct

sunlight condition with very good accuracy but it still cannot be functional in the bad

weather such as fog and snow. Therefore, radar is indispensable to compensate the

conditions that those two sensors cannot cover.
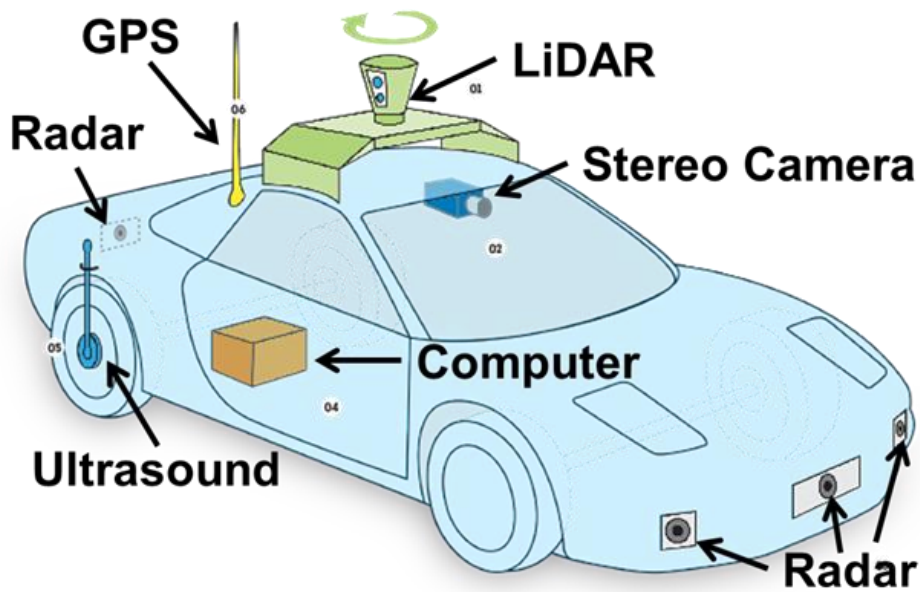
Fig. 1.1 Autonomous driving vehicle with sensors.

Nonetheless, there will be interference issues due to the multiple signals transmitted from the radars on the adjacent driving vehicles operating in the same area at the same time in the future autonomous driving system shown in Fig. 1.2[2]. Blue triangle is the sensing vehicle and the red circle shows nearest vehicles surrounding the sensing vehicle. Because the electromagnetic (EM) waves are totally reflected by the metal objects, the vehicles behind the red circle are blocked and will not affect the safety of the sensing vehicle. Nevertheless, there are still a red circle of vehicles affecting the detection of the sensing vehicle. Consequently, radar interference mitigation techniques will be essential in such multi-vehicle environment.
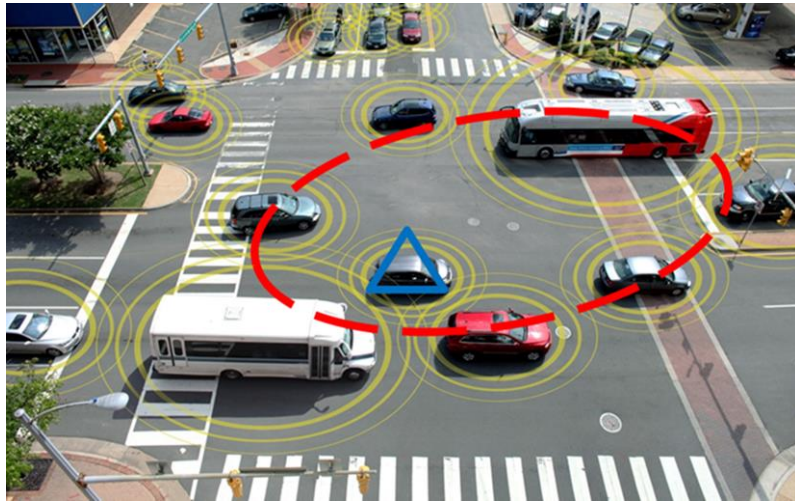
Fig. 1.2 Radar interference in future autonomous driving system.

There are several features that the commercial automotive radars need. First, wide bandwidth such as 1GHz is needed for high-resolution detection and localization of adjacent vehicles. Second, fully silicon-based such as SiGe is good for rapid popularization on behalf of its low-cost and highly-integrated features. Finally, linear FMCW modulation is feasible for low-power silicon implementation because of its constant envelop suitable for silicon power amplifiers. Many research works have already focused on providing the solution of highly-integrated silicon-based FMCW radar in the past [3]-[11]. In order to accurately detect and localize adjacent vehicles, several radars must be carried on each vehicle. A low-cost and highly-integrated CMOS radar could be the best candidate to fulfill this growing industrial need. There are several works demonstrating the feasibility of the CMOS technology in FMCW radar [12]-[14].

1.2　　Why Interference-Tolerant?

Fig. 1.3 shows the block diagram of the commercial automotive radar with linear FMCW modulation. It has a linear FM waveform generator to generate the triangular or sawtooth waveform and transmit out through a power amplifier (PA). The transmitting antenna radiates the EM waves (blue) to the target and the receiving antenna collects the reflected waves (green) from the target. The low-noise amplifier (LNA) amplifies the weak receiving signals and the mixer mixes the copied version of the transmitting signals (RF) and the amplified signals (RF_rx). The mixing signals downconvert to the IF and pass through the low-pass filter (LPF) to eliminate the unwanted noise. The Fast Fourier Transform (FFT) operation extracts the range and velocity of the target from the mixing signals.
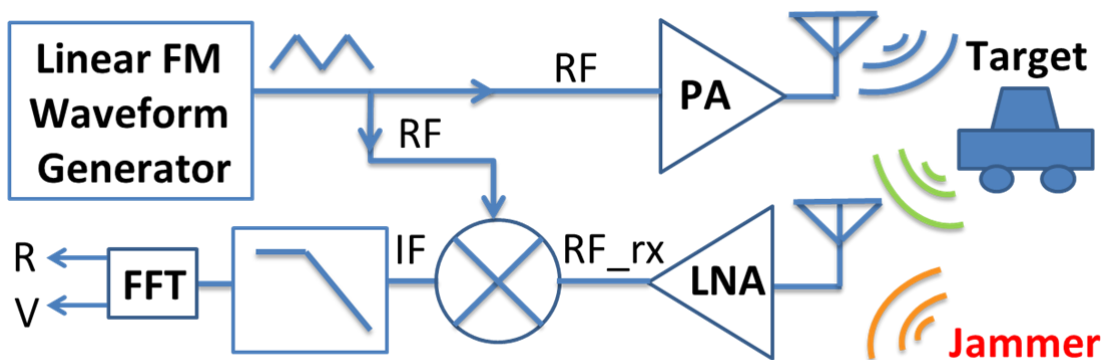
Fig. 1.3 Block diagram of the commercial automotive FMCW radar.
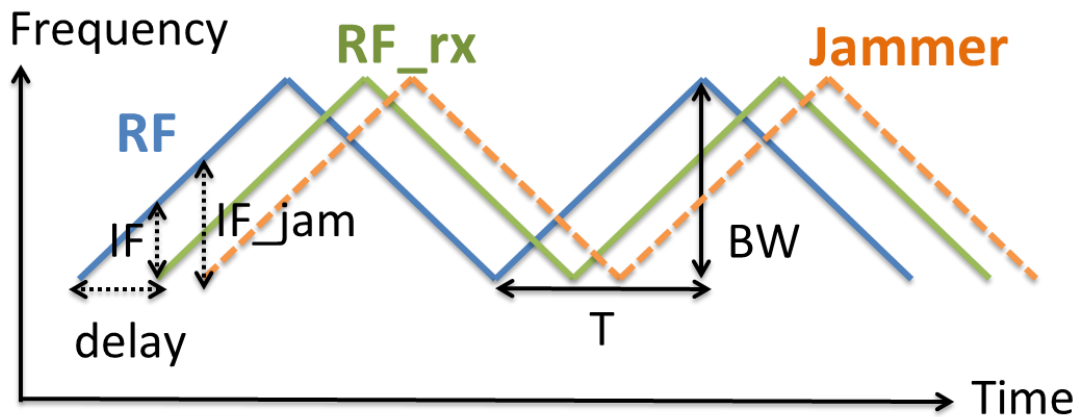
Fig. 1.4 Frequency modulation property of the FMCW radar.

The frequency modulation property of the FMCW radar shows in Fig. 1.4. The horizontal axis is time and the vertical axis is frequency. The frequency increases and decreases linearly with time and this pattern repeats every T second, which is the pulse repetition period. The maximum range of the frequency change is the FM bandwidth and it defines the slope of the frequency modulation when T is fixed. The blue curve (RF) is the transmitting FMCW signal and the green curve (RF_rx) is the receiving FMCW signal that has a delay corresponding to the range of the target. When mixing down at certain time, the frequency difference of these two FMCW signals is the IF signal. Using the IF signal and the slope calculated by BW/T can estimate the delay of the receiving signal by delay = IF ▪ T / BW. The range of the target is c ▪ delay / 2 because the EM waves travel twice of the range and the c is the speed of light.
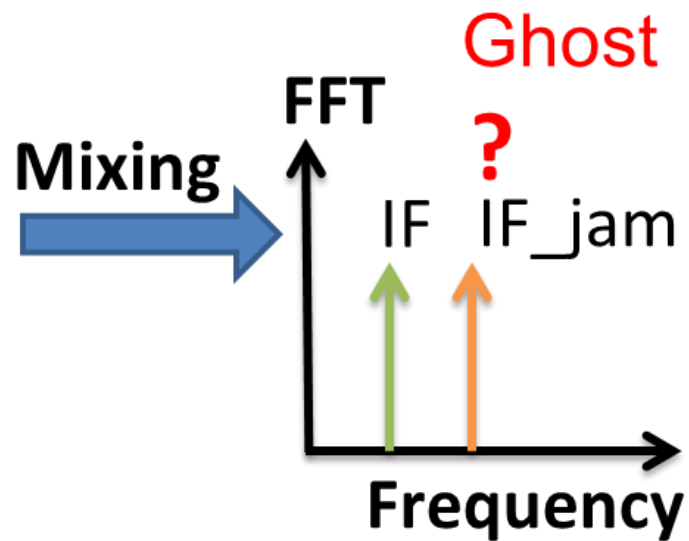
Fig. 1.5 FFT spectrum of the mixing signals with a jammer.

What if there is another FMCW radar appears as a jammer shown in Fig. 1.3. It generates the FMCW signal with the same frequency modulation pattern and transmits the EM wave (orange) to the receiving antenna of the victim. This jamming pattern has the same FM slope (orange) but different delay with respect to the receiving signal shown in Fig. 1.4. This jammer generates the interference IF_jam when it mixes down with the receiving signal. The FFT spectrum shown in Fig. 1.5 has two tones called IF and IF_jam and they cannot be differentiate which one is the target or jammer. Therefore, it is called ghost that appears in the FFT spectrum but there is no real target in front of the sensing vehicle with the range corresponding to the delay of the IF_jam frequency.
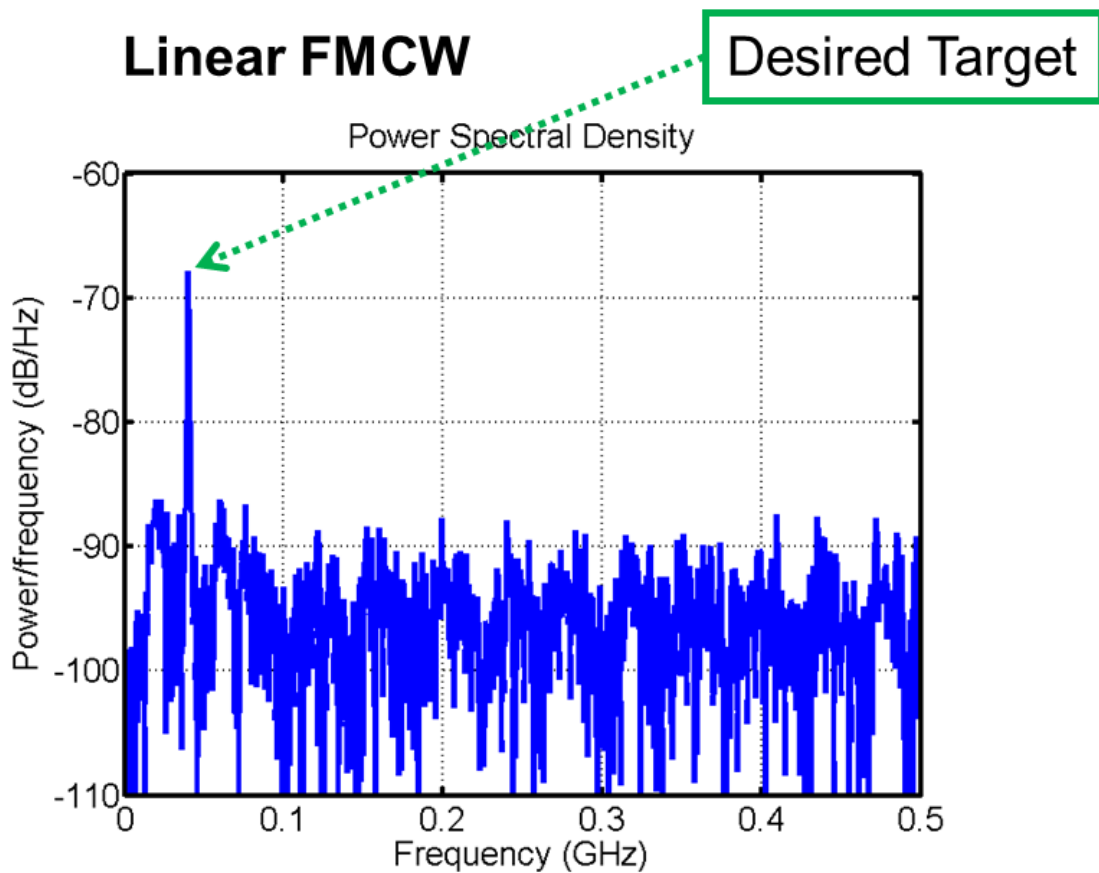
Fig. 1.6 (a) Simulation results of the linear FMCW radar: without jammer.

Fig. 1.6 shows the simulation results of the linear FMCW radar. The FFT spectrum has a peak corresponding to the range of the target shown in Fig. 1.6 (a). Therefore, it is a simple algorithm to estimate the range of the desired target by searching the peak position in the FFT spectrum. Fig. 1.6 (b) shows the simulation results when the jammer appears in the same linear FMCW radar. There is another peak showing up in the FFT spectrum next to the previous tone and it has similar amplitude if the range of the jammer is similar to the desired target.
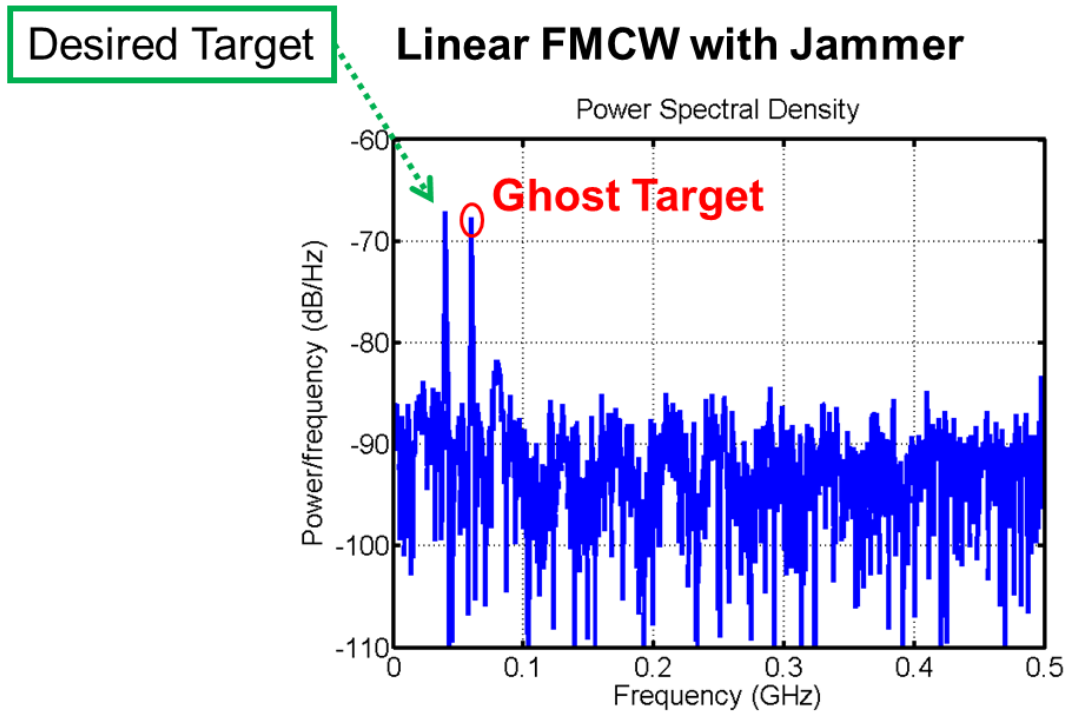
Fig. 1.6 (b) Simulation results of the linear FMCW radar: with a jammer.

In this case, the radar finds two targets when doing the peak search. However, there is actually no target at 60MHz, which might be the reflected EM waves from another linear FMCW radar. From this simulation, it could be foreseen that there will be many ghost tones in the FFT spectrum if many linear FMCW radars operate in the same arear at the same time in the future autonomous driving system. The main reason of this result is that both target and jammer use the same FM pattern which cannot be differentiated. Some interference mitigation techniques allocating frequency sub-bands at different time for different users to avoid concurrent frequency band usage have been reported in the past shown in Fig. 1.7 [15].
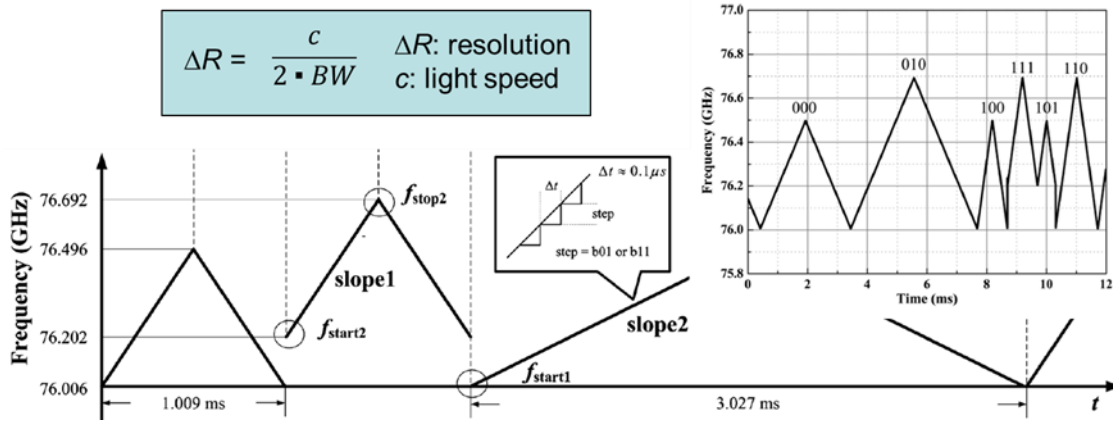
Fig. 1.7 FMCW radar with reconfigurable chirps.

Fig. 1.7 shows the reconfigurable chirps allocating sub-band for different users to avoid concurrent frequency band usage. There are three bits of different slopes in this system. However, it cannot use full FM bandwidth when operating at different slopes. From the equation of the range resolution, higher FM bandwidth has finer resolution; for example, 500 MHz is for 30cm resolution. Therefore, it scarifies the resolution if it cannot use the full FM bandwidth, especially when the number of users goes up. Fig. 1.8 shows the simulation results of this reconfigurable chirp radar system. In Fig. 1.8 (a), target and jammer use different chirps with different FM slopes. The left-hand side of Fig. 1.8 (a) shows the simulation results without the jammer where a peak can be easily recognized in the FFT spectrum. On the right-hand side, there is one jammer coexisting with the target and the results show that the peak is still visible and there is no ghost in the FFT spectrum.
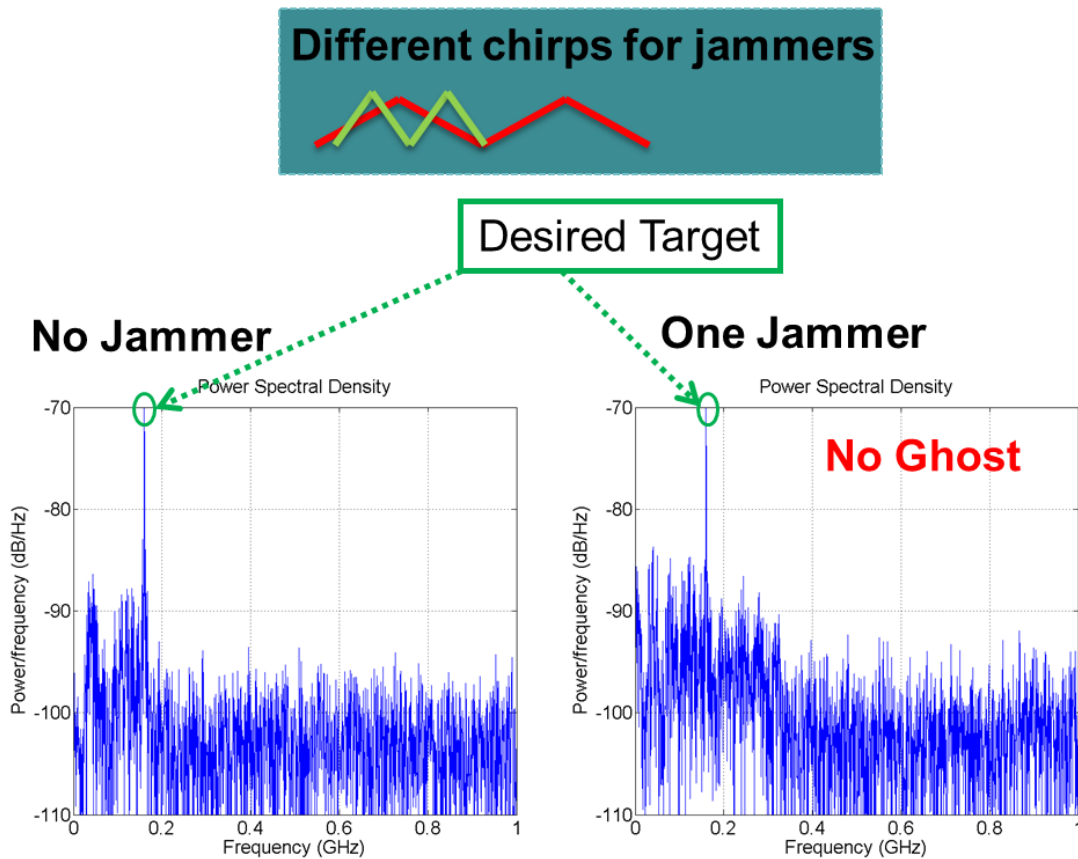
Fig. 1.8 (a) Simulation of the FMCW radar with reconfigurable chirps: without ghost.

Therefore, one jammer is tolerable in the FMCW radar with reconfigurable chirps, because the slopes are different so there is no single IF tone happening when these two slopes mixing down. Instead, the IF generated by the jammer spreads over the entire spectrum, which raises the noise floor within the FM bandwidth resulting in no ghost appearing shown in Fig. 1.8 (a). However, when the number of jammer increases and exceeds the capability of the reconfigurable chirp system, the ghosts start to show up even every jammer has different slopes.
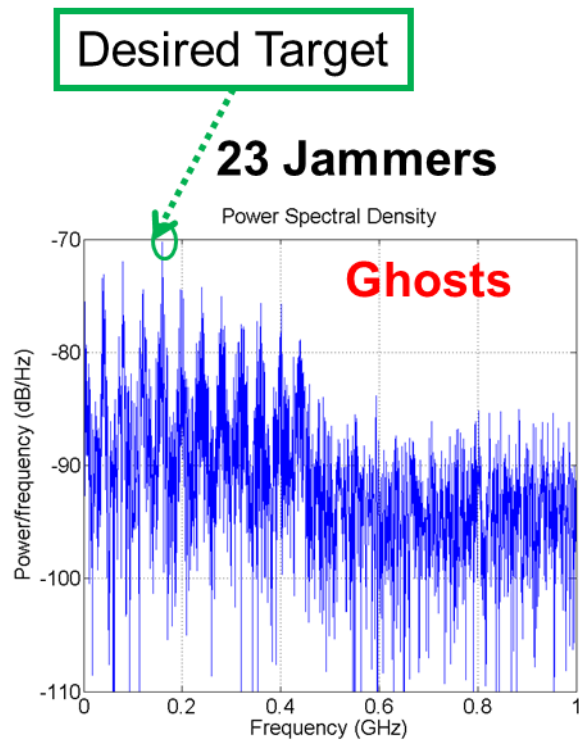
Fig. 1.8 (b) Simulation of the FMCW radar with reconfigurable chirps: with ghost.

Fig. 1.8 (b) shows a 23 jammers environment where many tones appear in the FFT spectrum and the desired target is overwhelmed by those ghosts. That is because, in certain case, the overlap frequencies from different chirps could also generate enough power at certain frequency and it produces a ghost at that frequency.

Therefore, the number of users trades off with the available bandwidth so does the range resolution in such reconfigurable chirp system. A technique allowing tens of radar interference with high range resolution is needed to solve such problem in future multi-user radar system.

1.3 Dissertation Organization

This dissertation presents the design and implementation of a one-coincidence code-division frequency hopping (FH) CW radar that can support up to 22 users with 1GHz bandwidth concurrently. Chapter 2 introduces the interference-tolerant multi-user radar system, including the operation principle, code-division frequency hopping radar system, and one-coincidence frequency hopping code. Chapter 3 reports the implementation and measurement results of this interference-tolerant multi-user radar system in detail. Chapter 4 concludes this dissertation.

Chapter 2

Interference-Tolerant Multi-User Radar System

2.1 Operation Principle

Fig. 2.1 shows the proposed one-coincidence code-division FH CW radar system block diagram. In the system, the code-division frequency hopping waveform generator generates the frequency hops based on different code sequences that replaces the conventional linear FMCW waveform. These frequency hopping waveform signals transmit out through the PA and transmitting antenna to the target. The transmitting signals are reflected from the target back to the receiving antenna and amplified through the LNA. The transmitting signals are also copied and delayed through the variable delay line and correlated with the receiving signals from the LNA. This correlator is actually consisted by a mixer and a LPF, which does the operation of the multiplication and the summation of those two signals. One is the known transmitting signal and the other is the delay version of this known signal. The range and velocity information can be extracted by the signal processing after the correlation process.
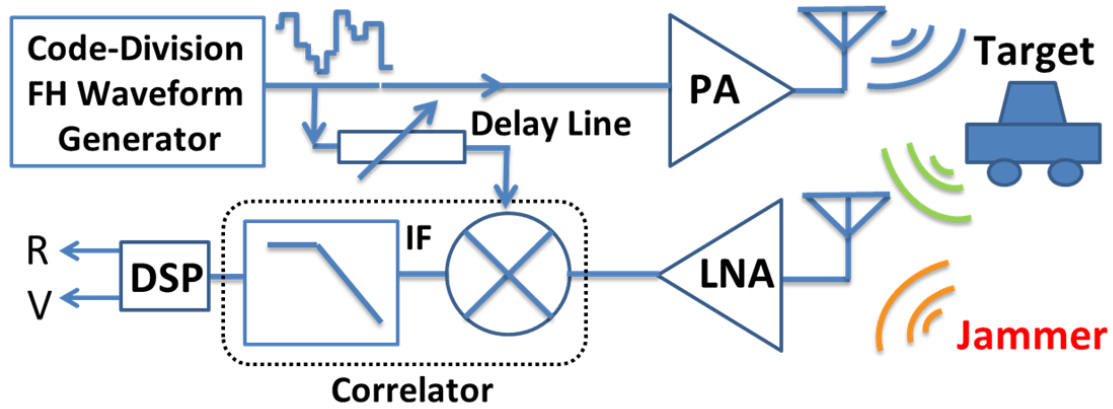
Fig. 2.1 Code-division FH CW radar system block diagram.

Fig. 2.2 shows the frequency modulation profile of this code-division FH waveform. The frequency is no longer linear with time; instead, it follows a specific code sequence to hop with time. The maximum hopping range is the overall system FM bandwidth of the radar and the sequence repeats every pulse repetition period. The blue curve (RF_delay) is the transmitting signal copied through the delay line, and green curve (RF_rx) is the receiving signal reflected from the target with the delay corresponding to the range of the target. These two frequency profiles have the same frequency modulation sequence because they are sent from the same code-division FH waveform generator. When sweeping the delay line until both waveforms matching to each other, it means the time delay matches with the time of the EM waves traveling to the target and back to the radar. Therefore, the range information can be calculated through this operation.
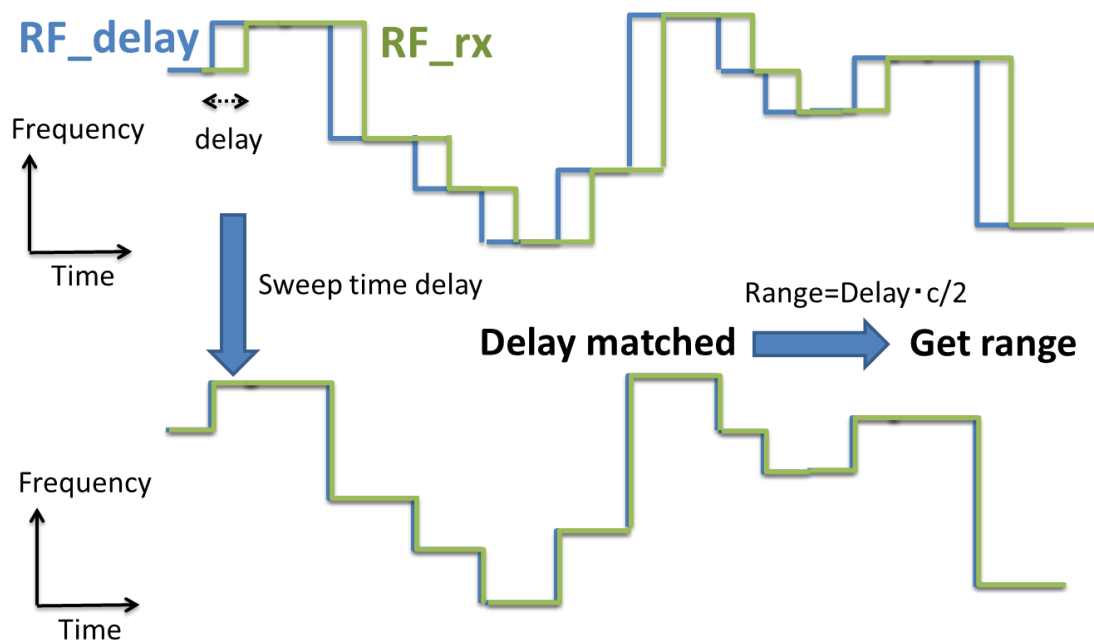
Fig. 2.2 Frequency modulation profile of the code-division FH waveform.

The operation principle of this code-division FH radar is shown in Fig. 2.3. First, Fig. 2.3 (a) shows a situation that the frequency codes do not align to each other. When these two frequency codes mix down, there is no signal in the desire baseband region because the mixing frequencies are different. The IF will locate at the spectrum with the frequency following the difference of the mixing frequency sequences. If there are N different frequencies in a code sequence, the N of the mixing signals will spread over the entire FM bandwidth of this radar system. Therefore, when integrating the signals in the desired region, there will be zero amplitude at this delay step other than the target delay.
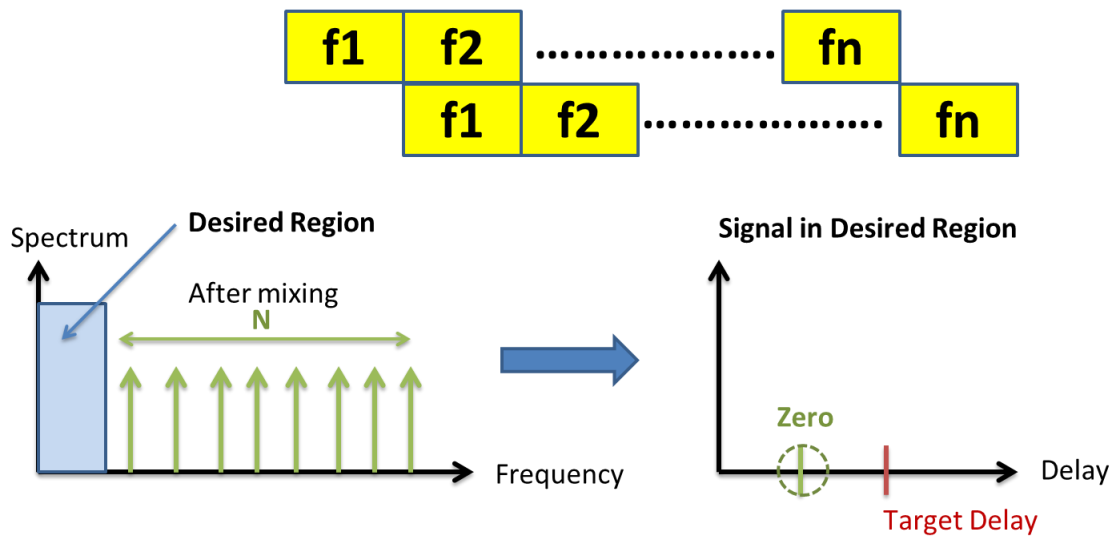
Fig. 2.3 (a) Operation principle of the code-division FH radar: frequency codes do not align to each other.

Fig. 2.3 (b) shows the situation when frequency code sequences shift by half period of the frequency hopping time. There is half overlap in each frequency code and this repeats N times, so there will be N times of signals in the desire region but with half power comparing to the case shown in Fig. 2.3 (a). The other N times of signals spreading out of the FM spectrum other than the desired region have another half power. When summing up both of the power inside and outside the desired region, the overall power equals to the previous case where the delay shift is one period. When integrating signals in the desire region, there will be an amplitude at this half period time delay, which can be speculated as half of the amplitude at the target delay.
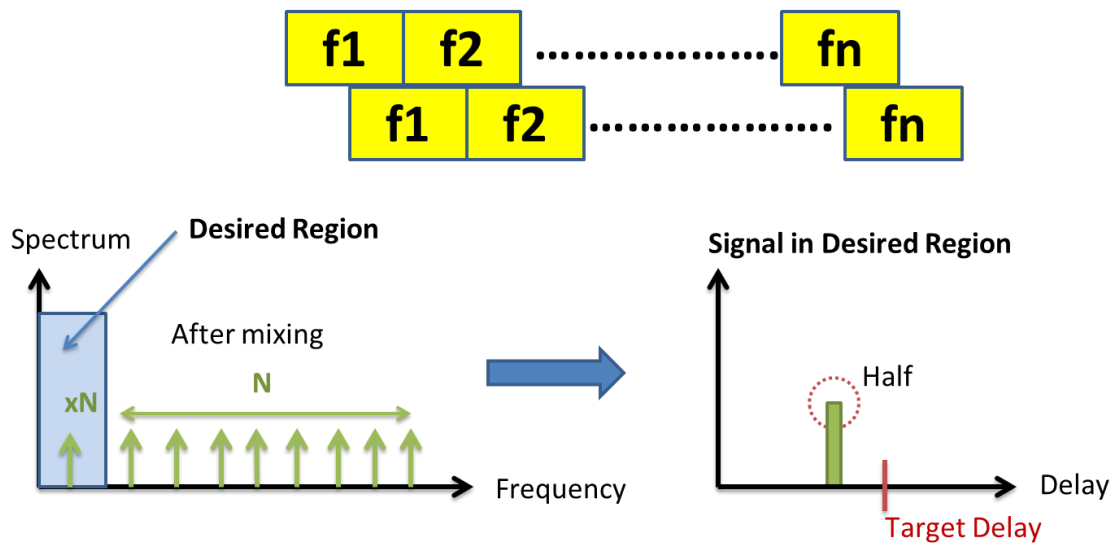
Fig. 2.3 (b) Operation principle of the code-division FH radar: frequency codes

shift by half period.

Fig. 2.3 (c) shows the situation when two frequency hopping code sequences align

to each other. In this case, all the IF signals will be in desire region after mixing

operation, and there will be zeros elsewhere in the FM spectrum because any two

frequencies are the same in each time slot. When integrating the signals inside the

desired region, there will be a peak at the time delay matching to the target delay. This

peak has the amplitude that is twice of the amplitude when the frequency hopping codes

shift by half of the period. Therefore, the range information can be extracted through the

delay line step where is the pick location in the sweeping operation shown in Fig. 2.3

(d). When integrating the signals in desired region at different delay line shift, it
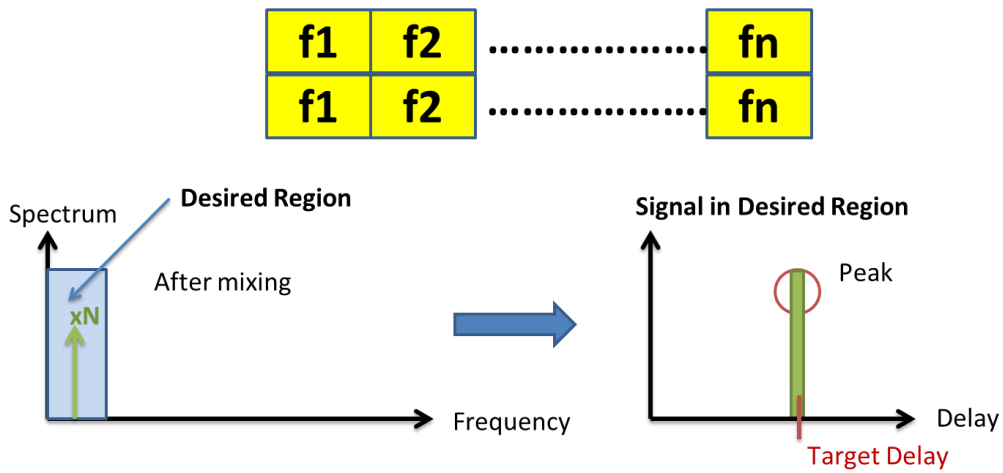
Fig. 2.3 (c) Operation principle of the code-division FH radar: frequency codes

align to each other.

generates a profile from zero to the peak and goes back to zero. This amplitude profile

corresponds to the delay that is away from or closed to the true target delay.
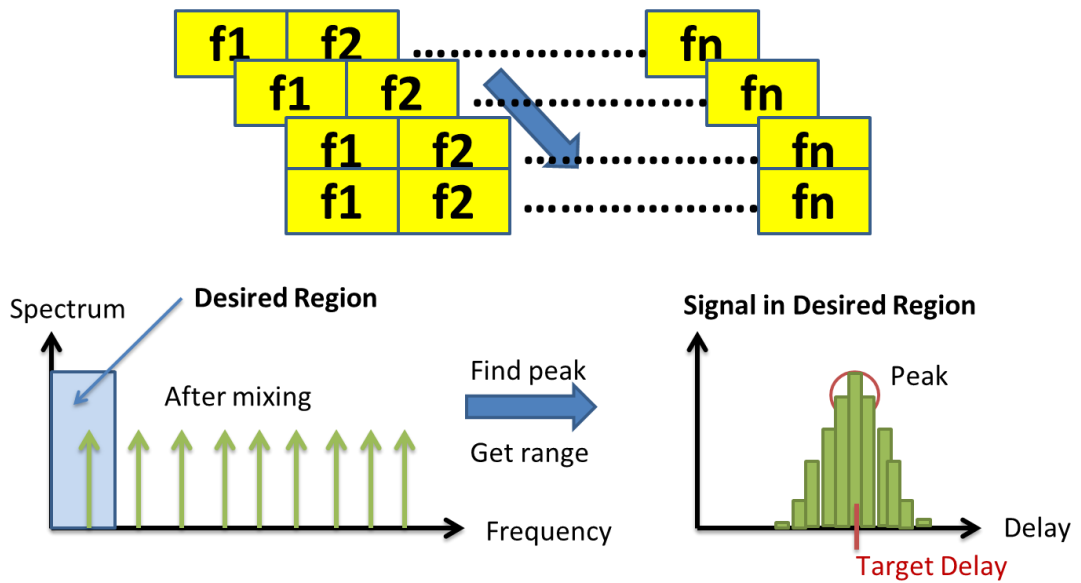
Fig. 2.3 (d) Operation principle of the code-division FH radar: sweeping delay.

What if a jammer appears? If there is a jammer (orange) shown in Fig. 2.1 using a code-division FH radar but with different code sequence so as the frequency hopping waveform shown in Fig. 2.4. This jammer has different frequency modulation profile other than the target, so it is not a delay version of the transmitting signal like RF_delay or RF_rx. When sweeping the delay line to match the delay of these two signals (RF_delay and RX_rx), the target delay matches to the delay line step and the FM profile coincide with each other. However, the jammer never has overlap of the FM profile no matter how many steps that the delay line sweeps. Therefore, the range information can be extracted correctly even receiving the signal with a jammer.
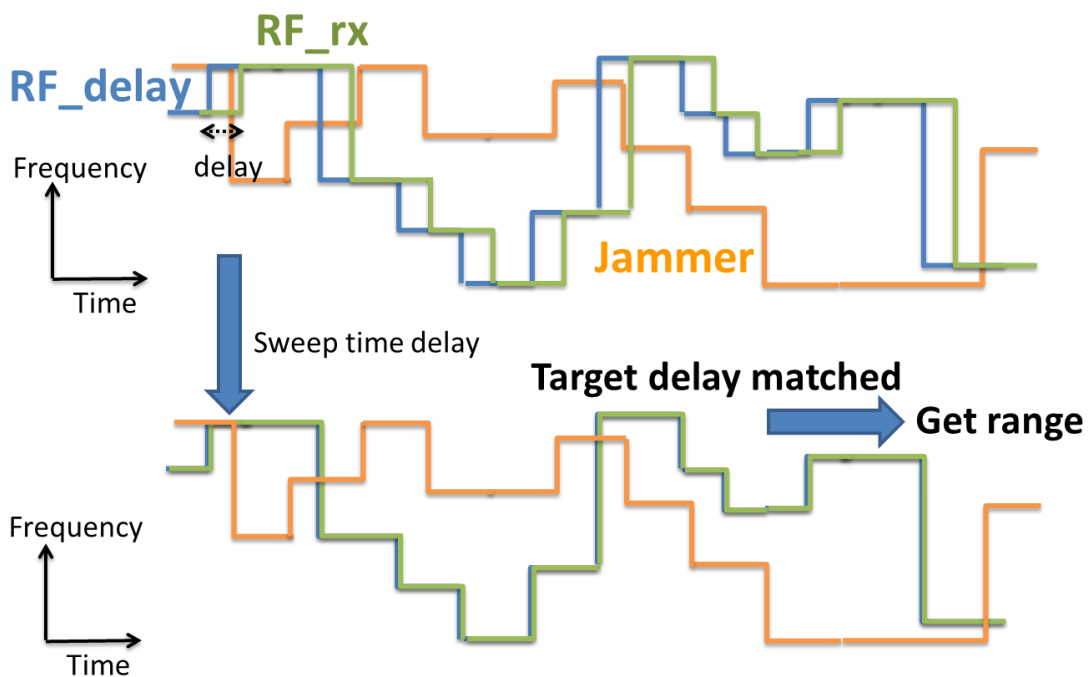
Fig. 2.4   When a jammer appears with different FH code sequence.
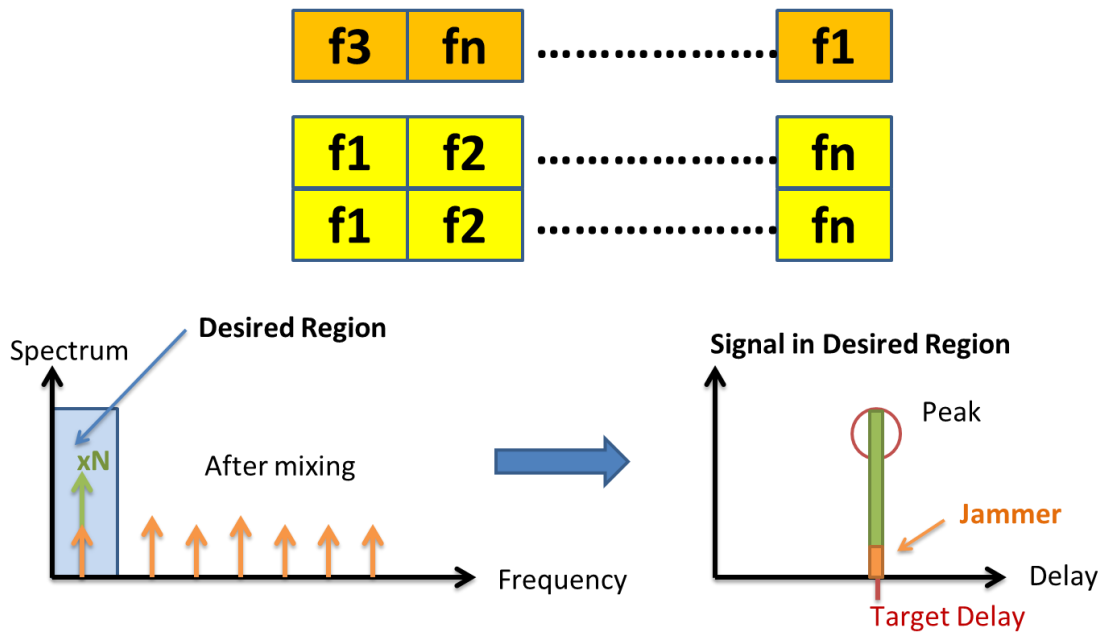
Fig. 2.5 (a) Jammer-tolerant mechanism: frequency codes align to each other but jammer does not.

Fig. 2.5 explains the mechanism of such jammer-tolerant operation. A jammer has the same frequency modulation range but with different frequency hopping code sequence in orange color shown in Fig. 2.5 (a). When the delay line step matches to the target delay, the target signal has N times power residing in the desire region. On the other hand, the jammer does not match to the transmitting frequency code sequence, so the IF signals spread over entire spectrum after mixing operation. When integrating the signals inside the desired region, the target has a peak at the delay line step matching to the target delay but the jammer only has a small amount comparing to the target.
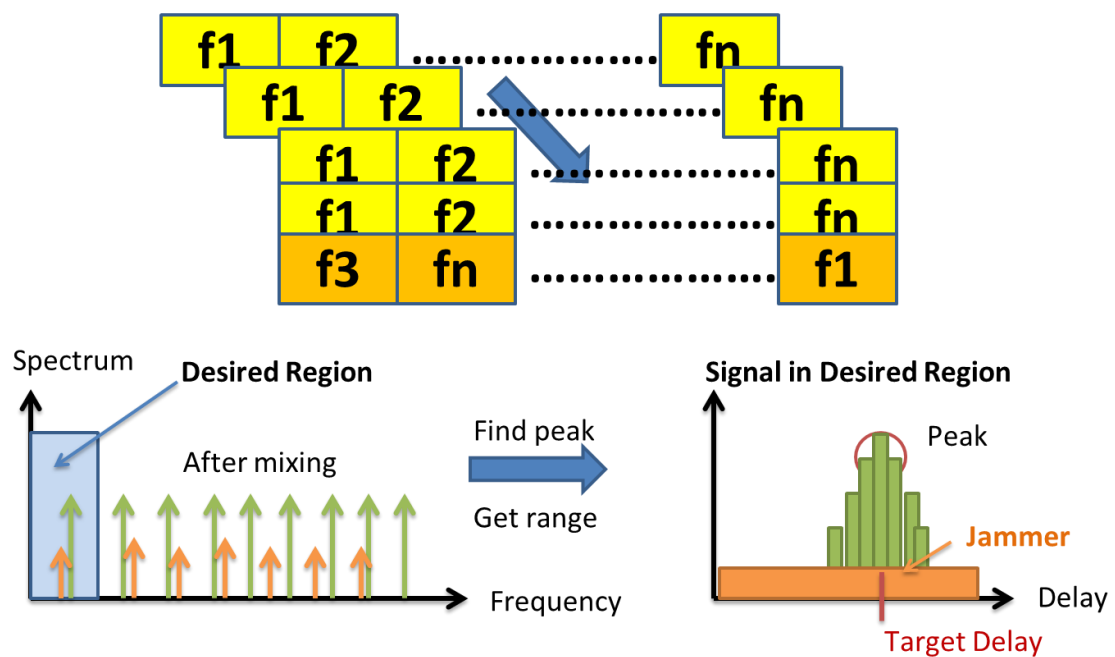
Fig. 2.5 (b) Jammer-tolerant mechanism: sweeping delay line when a jammer appears.

Fig. 2.5 (b) shows the results of sweeping the delay line steps. The IF signal power of the target inside the desired region increases when the delay line step approaches to the target delay; on the contrary, the IF signal power of the jammer does not. After integration, target signal has the mountain shape of amplitude profile with a peak at the target delay. However, the jammer spreads out like white noise if assuming N is big enough so that the overlap can be minimized. Therefore, the range information can still be extracted from the jammer when the delay line sweeps to the target delay, which is because the peak amplitude is N times larger than the jammer.

2.2 Code-Division Frequency Hopping Radar System

In order to design a new system, the first step is to define the system parameters or the specs. The key spec is the bandwidth because the resolution can be calculated by:

$$dR = \frac{c}{2 \cdot BW} \, , \qquad dR: resolution, \quad c: light \; speed. \qquad (2.1)$$

First, choosing 500MHz as the FM bandwidth has the resolution equal to 30cm. Second, setting the number of frequency steps to 25 has $10^{\wedge 25}$ different frequency codes , which is a very big number of the combination. Third, choosing the length of frequency code sequence as 1.25us, which corresponds to 188m unambiguous range, is long enough for the mid-range automotive radar. The unambiguous range relates to the pulse repetition time PRT by:

$$R_{max} = PRT \cdot c \, /2, \qquad PRT: pulse \; repetition \; time. \qquad (2.2)$$

Because the frequency code sequences repeat every PRT seconds, the maximum delay line steps of the system is PRT so as the maximum detection rage. When the target locates farer than this range, it generates another tone every PRT second.

Fig. 2.6 Simulation of the frequency hopping system with $N = 25$.

Fig. 2.6 shows the simulation results of the frequency hopping system with 25 frequency steps. The frequency hops with time and there are 25 non-overlapping frequency steps, which form a pulse used for the radar detection. These 25 frequency steps equally occupy the total FM bandwidth of 500MHz from 24GHz, so each has 20MHz sub-channel bandwidth. The frequency code jumps back to f_1 every 25 steps so that the target cannot be identified if the traveling time of the radio wave is larger than a pulse PRT. A segment of the frequency hopping waveform is shown in Fig. 2.7. It is a unique waveform for each different code sequence.

Fig. 2.7   A segment of the frequency hopping waveform.

Fig. 2.8 shows the simulation spectrum of the code-division FH signal shown in

Fig. 2.6. The FFT operation applies to a frequency hopping pulse containing the entire

code sequence of 25 frequency steps. The frequency domain signal is similar to a

500MHz OFDM signal because both of them contain 25 frequencies within 500MHz

bandwidth. When zooming into the in-band spectrum of the frequency hopping signal

shown in Fig. 2.8 (a), the sub-channel of one frequency step can roughly be found out

and there are 25 of them shown in Fig. 2.8 (b).

24
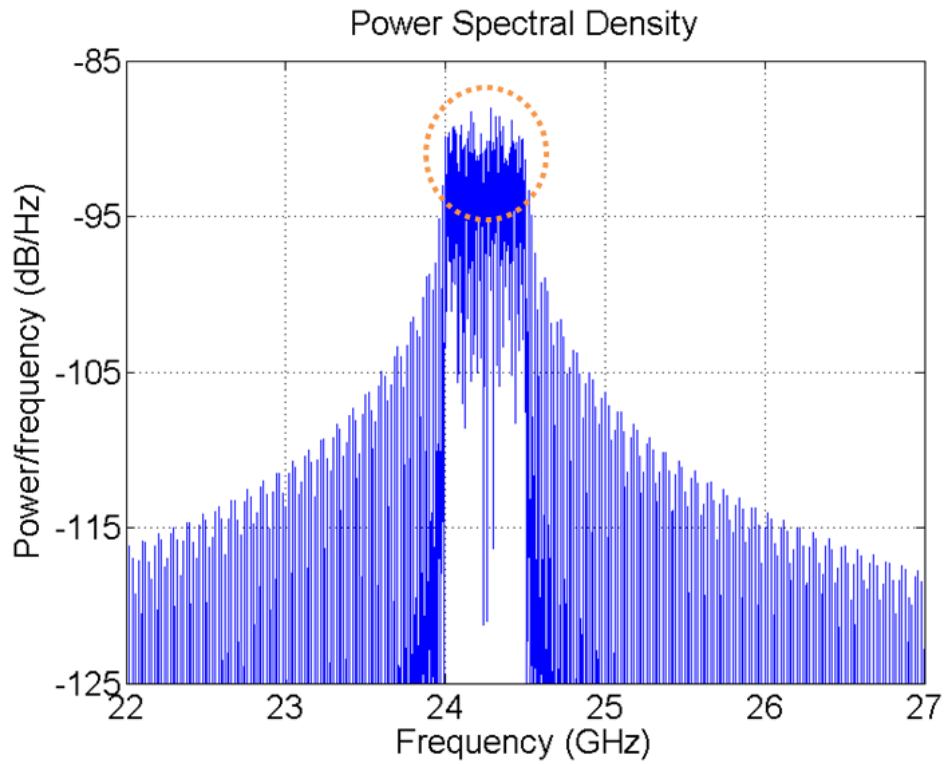
Fig. 2.8 (a)   Simulation spectrum of the code-division FH signal: whole view.
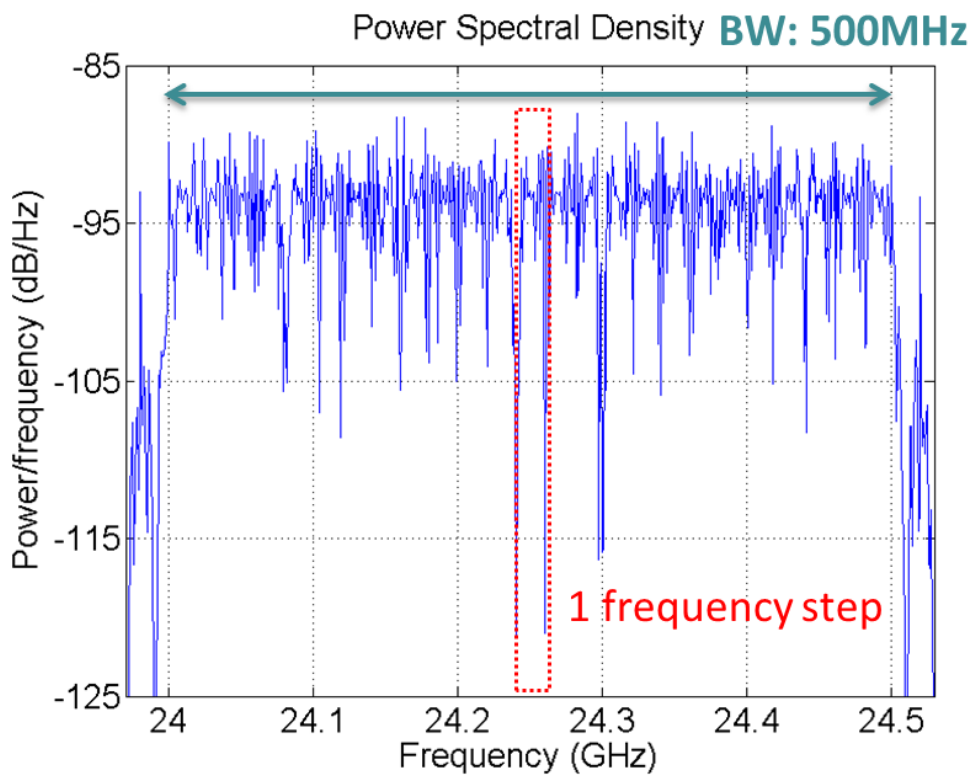
Fig. 2.8 (b)   Simulation spectrum of the code-division FH signal: enlarged view.
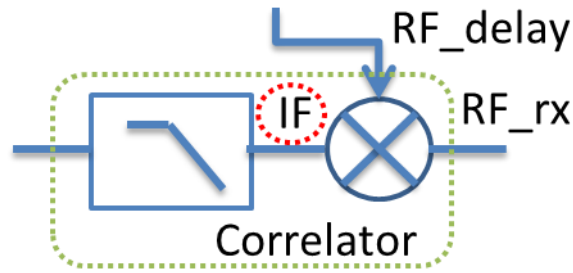
Fig. 2.9   Mixing signals of two FH signals with the same code.

When two frequency hopping signals with same code mix together shown in Fig. 2.9 as follows:

$$IF = RF\_delay \cdot RX\_rx. \tag{2.3}$$

If both frequency code sequences do not align to each other, which means there are different frequencies to mix down, the IF would have the sinusoid signals with different frequencies. Fig. 2.10 shows the simulated IF waveform of the mixing signal from RF_delay and RX_rx after the mixer. Fig. 2.10 (a) shows the situation that two code-division frequency hopping signals do not align to each other. The waveform of the IF mixing signal has the average value of zero, which means the DC value is also zero. Fig. 2.10 (b) shows the situation that two code-division frequency hopping signals align to each other. There is an average value and this value is not zero.

Fig. 2.10 (a)   Simulated IF waveform of the mixing signal: two code-division

FH signals do not align to each other.
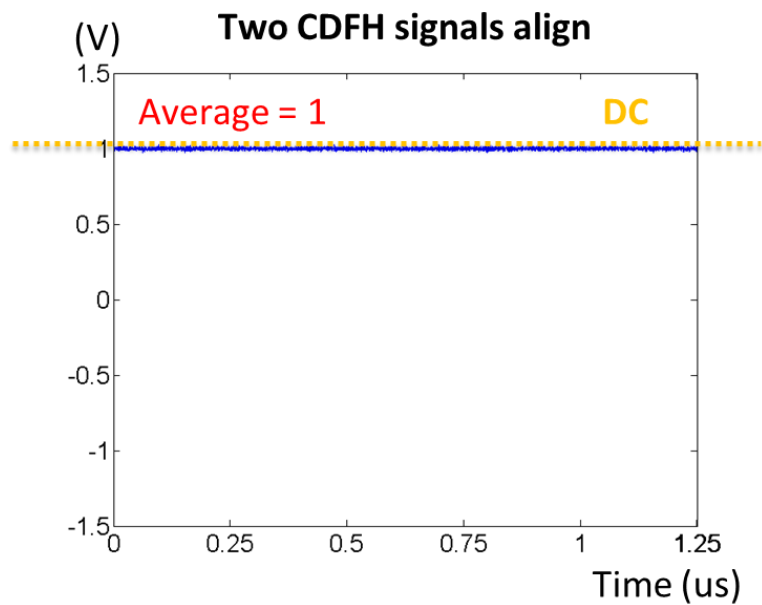
Fig. 2.10 (b)   Simulated IF waveform of the mixing signal: two code-division

FH signals align to each other.

27

Fig. 2.11 examines the simulation results of the mixing IF signal from two code-division frequency hopping sequences shown in Fig. 2.9 in frequency domain. Fig. 2.11 (a) shows the case that two codes do not align to each other. The mixing of different frequency codes produces the IF frequencies spreading over the available FM bandwidth. If two frequency hopping sequences align to each other shown in Fig. 2.11 (b), there is a peak at DC. These two frequency domain results are in line with the time domain results shown in Fig. 2.10.
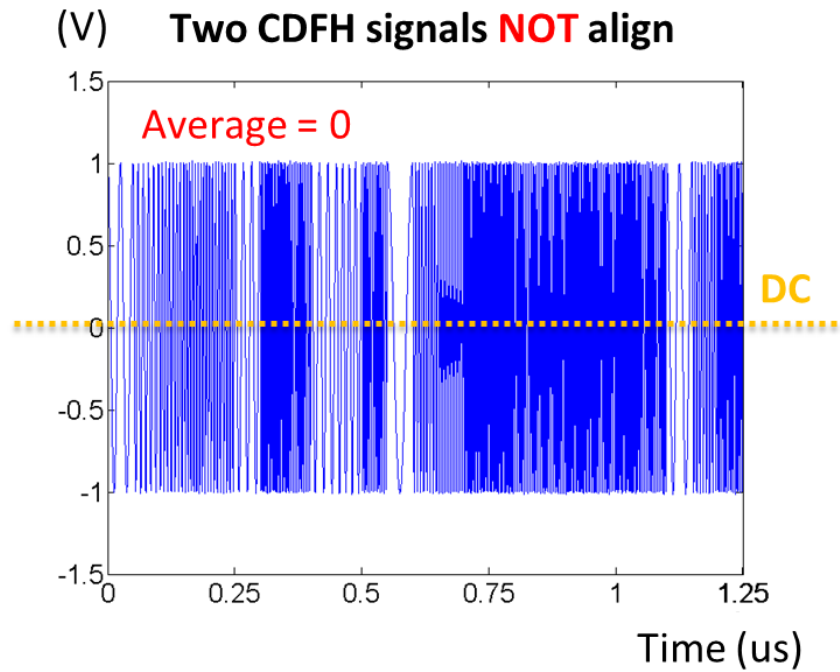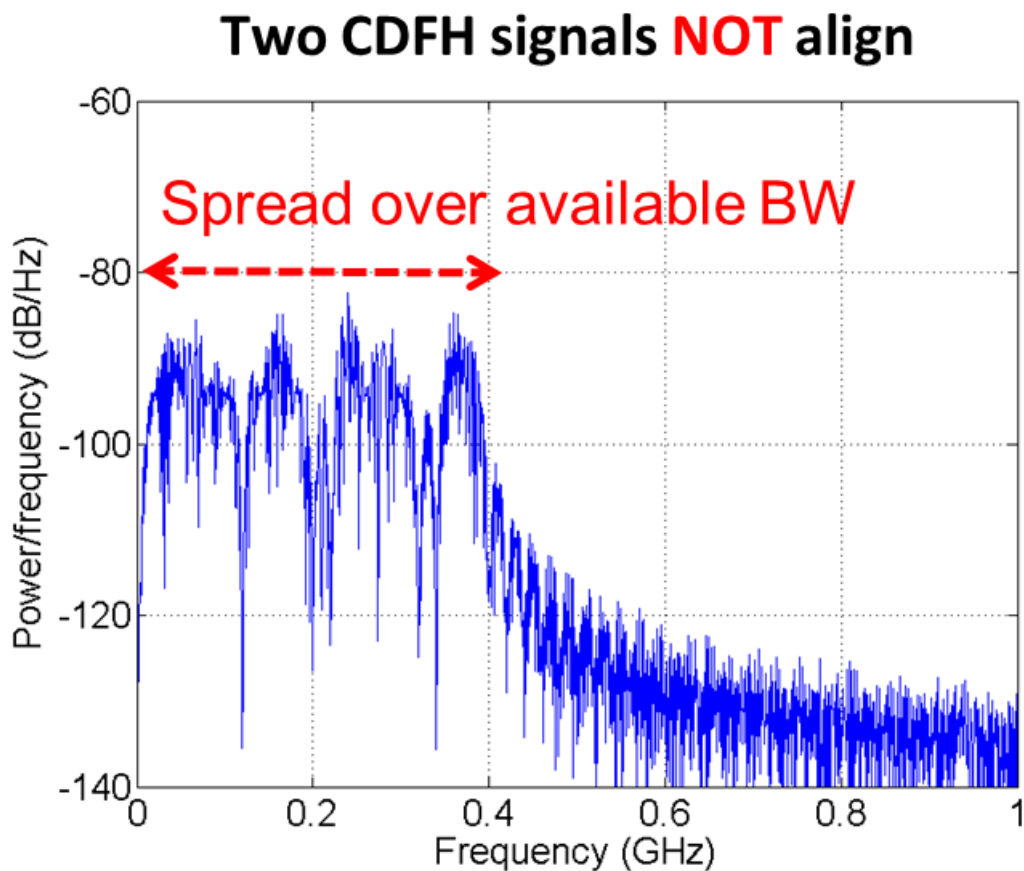

Fig. 2.11 (a) Simulated IF spectrum of the mixing signal: two code-division FH signals do not align to each other.
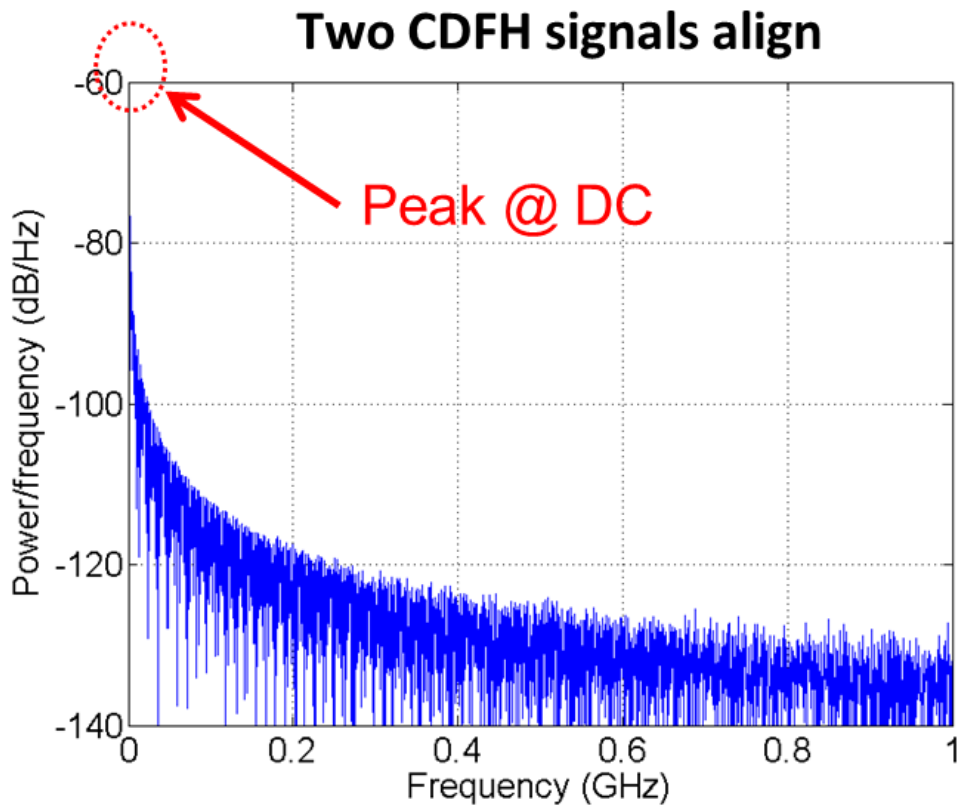
Fig. 2.11 (b)   Simulated IF spectrum of the mixing signal: two code-division FH

signals align to each other.

When the mixing signals pass through the LPF shown in Fig. 2.12, this is actually

a correlator output result as follows:

$$BB(\tau) = \sum_{t=0}^{\tau} \left(RF_{delay}(t - \tau) \cdot RF\_rx(t) \right). \tag{2.4}$$

When sweeping the delay line steps, there is a peak at target delay in the correlation plot

shown in Fig. 2.13. The target range can be calculated from this delay.
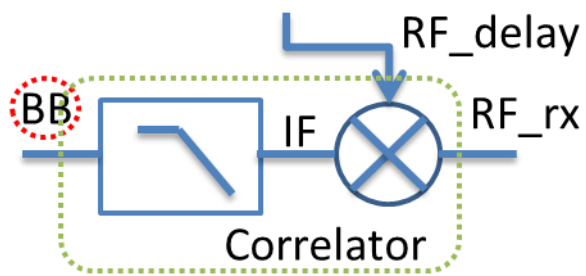
Fig. 2.12   Mixing signals pass through the LPF.

For example, in Fig. 2.13, the correlation peak locates at 100ns and the corresponding

range of this delay is 15m.
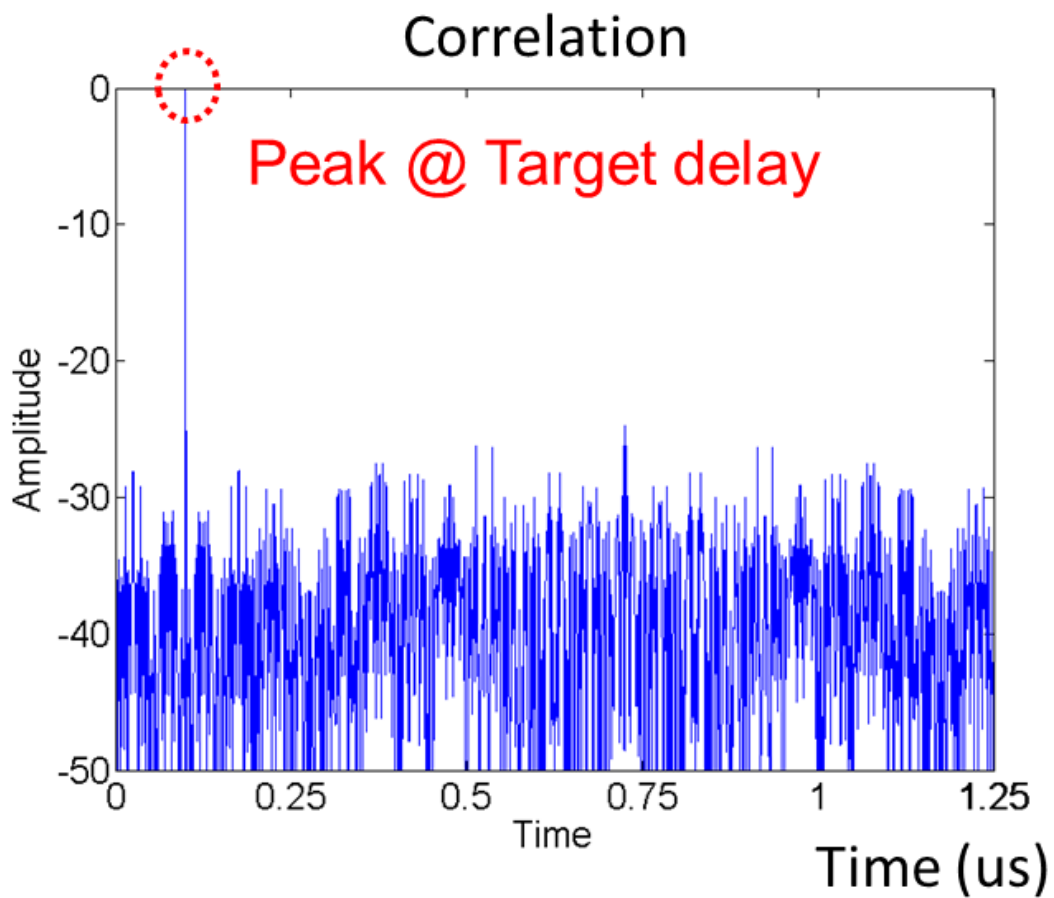
Fig. 2.13   Simulated correlation plot of the code-division FH signals.

Fig. 2.14 shows the resulting waveform when the code-division frequency hopping radar receives target and jammers all together. There are 23 jammers generated by a code generator with pseudo-random permutation of *N*. The receiving signals combine the target with all of 23 jammers so that it is impossible to distinguish the target signal and jamming interference from the waveform. However, the target can still be extracted from this noise-like waveform after the correlation operation shown in Fig. 2.15. The jammers spread over the entire spectrum, which only raises the noise floor but does not affect the peak detection of the code-division frequency hopping radar.
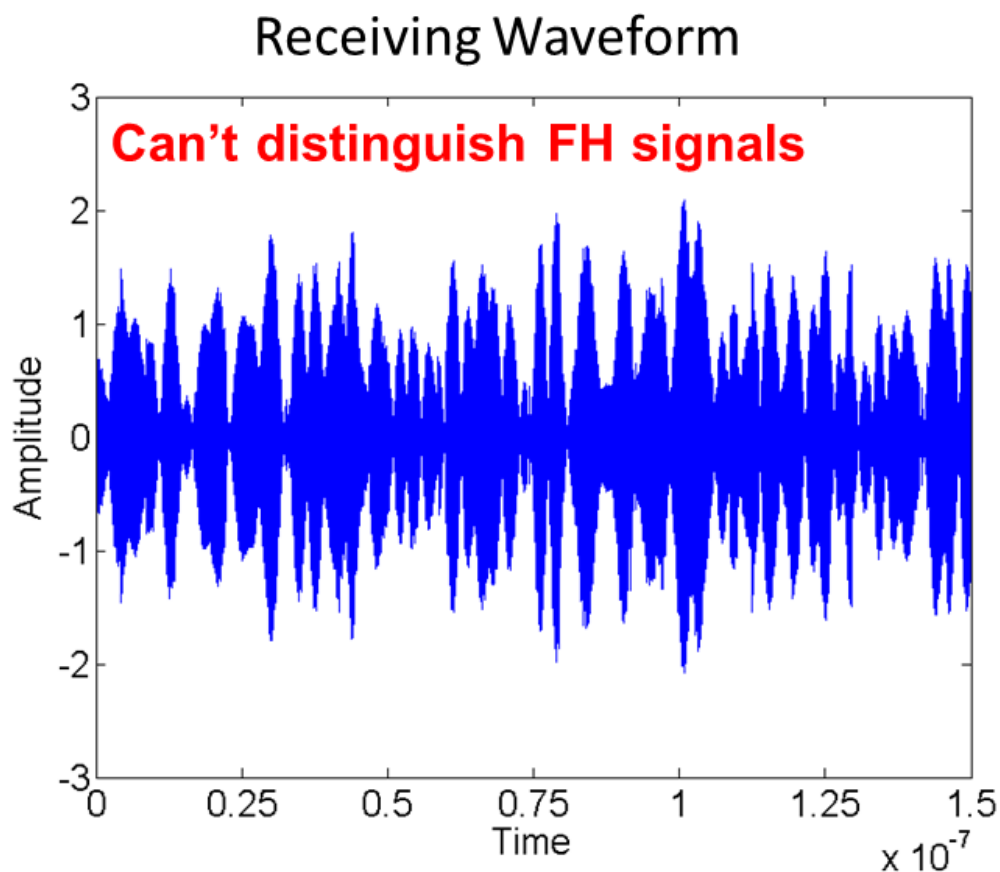
Fig. 2.14   Receiving waveform of the target with 23 jammers.
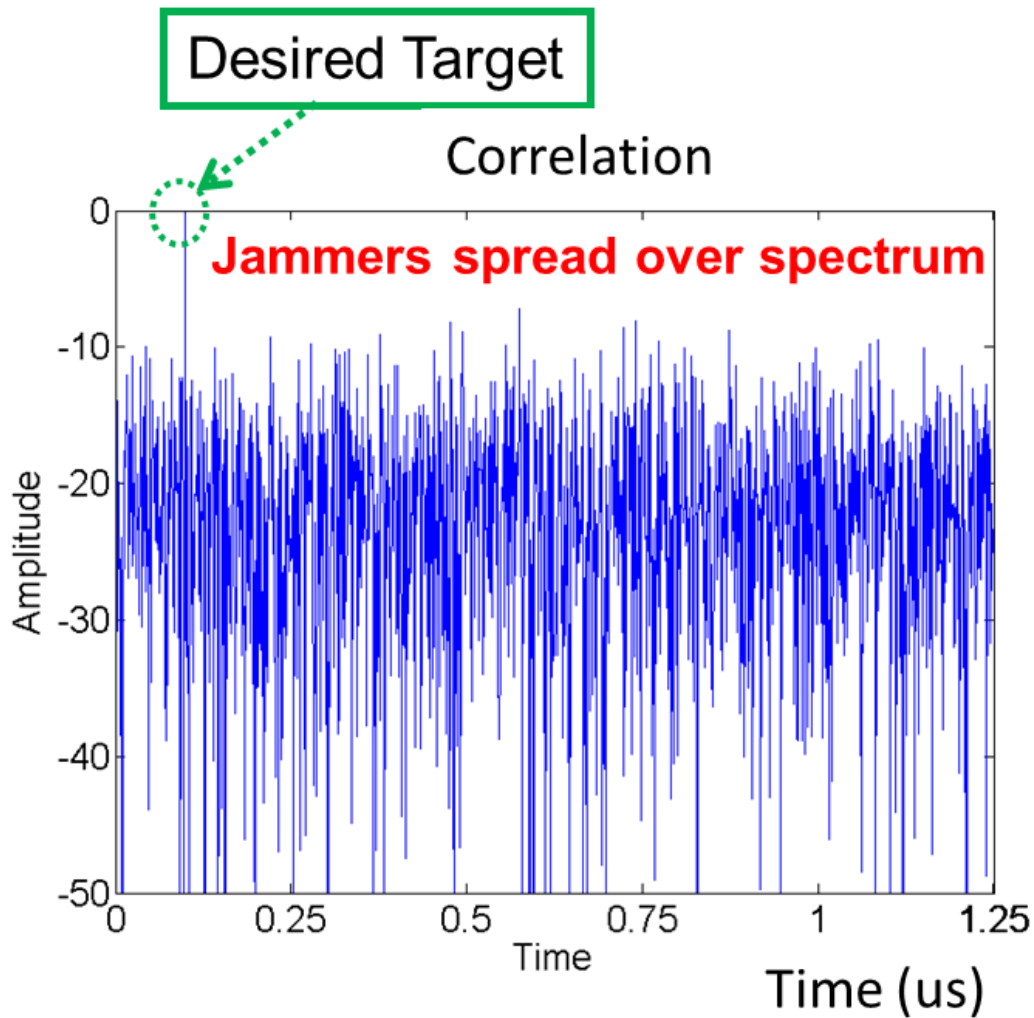
Fig. 2.15 Simulated correlation plot of the target with 23 jammers.

Is there any possible situation that it may generate the ghost to ruin the detection of

the radar if N is not big enough in the pseudo-random permutation codes? Yes, if the N

is not big enough, there might be certain case that the frequency codes from different

users overlap in a certain period with certain amount of power. Fig. 2.16 shows a

manipulated case that there are 24 users with one as target and 23 as jammers among

them. When receiving all of them, the first and last frequency codes, in certain time

delay, coincide in this manipulated case. In this case, a ghost happens shown in Fig. 2.17. There is still a peak in the correlation plot, but another bigger peak shows up as ghost that is due to the jammers. Although the probability of this case happening is low, it somehow will happen because of the randomness. Furthermore, it makes the radar have the wrong detection and affects the safety. Therefore, a well-defined sequence is needed to quantify the interference-tolerant performance.

24 Users Code-Division FH Radar System

Frequency Codes Overlap

f1, f2 ,..., f7, f25 → Target

f1, f9 ,..., f14, f25 ⎤

f1, f12,..., f9, f25 ⎬— 23 Jammers

⋮

f1, f22,..., f2, f25 ⎦
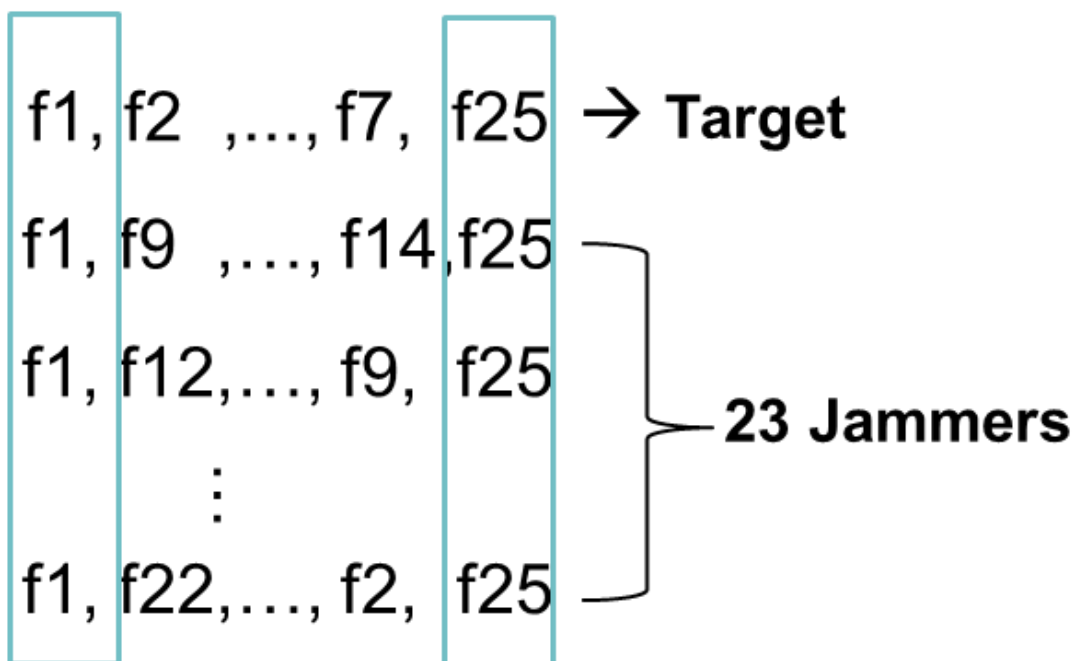
Fig. 2.16　A manipulated case that will generate a ghost.
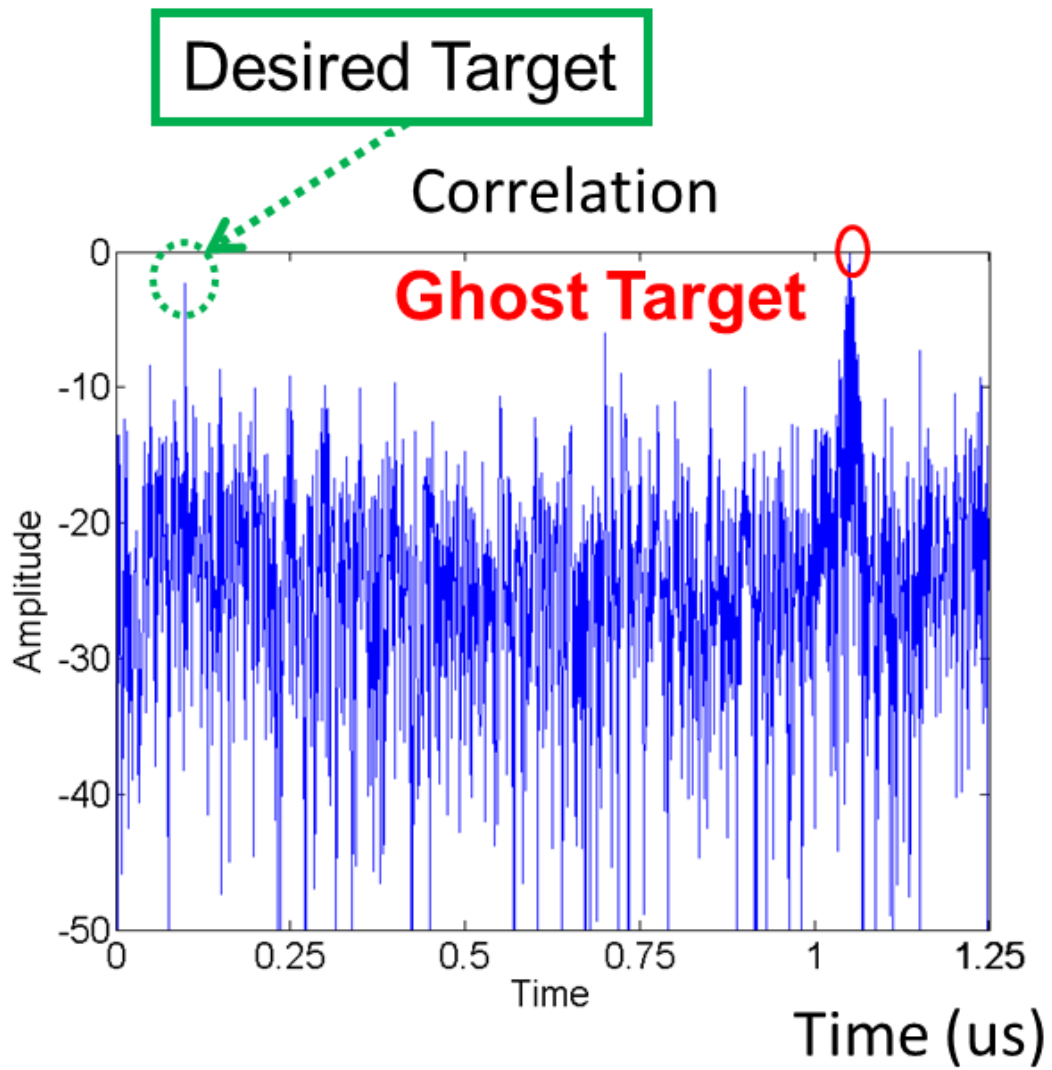
Fig. 2.17 Simulated correlation plot of the manipulated case in Fig. 2.16.

2.3   One-Coincidence Frequency Hopping Code

FH is a spread-spectrum (SS) technique that has been used in Bluetooth for multi-user multiplexing. Every user follows a sequence of frequency to hop with time. When two users occupy the same frequency channel concurrently, the coincidence or a hit happens and it results in mutual interference. One-coincidence sequence has the property that the maximum number of hits between any pair of sequences belonging to the set is one [16].

2.3.1   Frequency Hopping Signal

Frequency hopping signal has the following properties shown in Fig. 2.18. The signal length is T seconds constructed by N frequency steps with total bandwidth B. All the frequencies are non-repeating and each frequency appears exactly once within T seconds with sub-channel bandwidth as B/N. The frequency of kth time slot, f_k, is frequency modulated with respect to the carrier frequency f_0 by:

$$f_k = f_0 + y_i(k) \cdot (B/N), \qquad k = 0, 1, \dots, N-1. \qquad (2.5)$$

where, $y_i(k)$ is the placement operator which are sequence of integers called FH code.
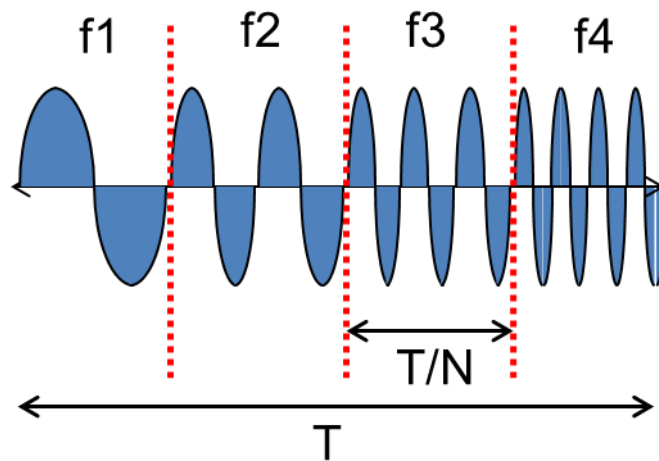
Fig. 2.18 Frequency Hopping Signal.

Choosing yi(k) as the pseudo-random permutation of N is an intuitive solution, but it cannot have consistent performance when N is not big enough. Therefore, a well-defined sequence is needed to quantify the interference immunity performance.

2.3.2   Hamming Correlation

The mutual interference happens when two users occupy the same frequency channel concurrently. For a multi-user frequency hopping system, a coincidence or a hit is when two users occupy the same sub-frequency channel. A one-coincidence sequence is defined as the maximum number of hits between any pair of sequences belonging to the set is one. If a code-division frequency hopping system has 25 steps, there is only one hit from 25 sub-frequencies.

The most common radar receiver is a matched filter or correlator, correlating the reference signal with the receiving signal. The receiving signal is the delayed version of the reference signal reflected from the target. The target can be identified through the peak position of the auto-correlation function, corresponding to the traveling time of the EM wave. On the other hand, the mutual interference between different users can be quantified by cross-correlation function. The interference immunity performance of FH code can be evaluated by periodic Hamming correlation function $H_{XY}(\cdot)$, defined as follows:

$$H_{XY}(\tau) = \sum_{i=0}^{N-1} h(X_i, Y_{i+\tau}) \ , \ 0 \leq \tau \leq N-1. \tag{2.6}$$

$$where \quad h(X_i, Y_{i+\tau}) = \begin{cases} 0, & X_i \neq Y_{i+\tau} \\ 1, & X_i = Y_{i+\tau} \end{cases}$$

The above equation defines the auto-correlation function $H_{rr}(\tau)$ when $r = s$, and cross-correlation function $H_{rs}(\tau)$ when r ≠ s. From this equation, the results have a one when two codes coincidence at certain time. If there is no coincidence, the results have a zero. The final result is the summation of those ones and zeros for the entire sequence of codes. The maximum non-trivial correlation value is defined as:

$$H_{am} = max\{\, H_{rr}, \tau = 1,\ \ldots\ ,\ N-1\,\} \tag{2.7}$$

and

$$H_{cm} = max\{\, H_{rs},\ r \neq s\ ,\ \tau = 0, 1\ ,\ \ldots\ ,\ N-1\,\} \tag{2.8}$$

The H_{am} is for auto-correlation, and it is zero ideally besides the peak. The maxima among those non-zero values quantifies the performance of the sequence. The H_{cm} is for cross-correlation, and it is one ideally in a one-coincidence sequence. Therefore, for a FH code set S, the optimal Hamming correlation pair of S is $(H_{am}, H_{cm}) = (0, 1)$. That is, one-coincidence FH sequence.

2.3.3 Extended Hyperbolic Congruential Code

One of the popular methods to construct a FH code set is to use a congruential equation. EHC code is a one-coincidence sequence with optimal Hamming correlation property $(H_{am}, H_{cm}) = (0, 1)$ [17]. Its placement operator, $y_i(k)$, is defined as:

$$y_i(k) \equiv \begin{cases} (\,i \cdot k\,)^{-1}\ mod(p), & k = 1, 2,\ \ldots\ ,\ p-1; \\ 0, & k = 0. \end{cases} \tag{2.9}$$

where p is a prime number greater than two, k is the time slot, and i is the user identification number from $\{1, 2, \cdot\cdot\cdot, p-1\}$. By choosing $N = p$, an EHC code set

contains $N-1$ different codes for $N-1$ users. Each EHC code has N different

frequencies occupying N continuous time slots, and its auto-correlation peak is $H_{xx} = N$

with $H_{am} = 0$. This is due to choosing p as a prime number that sets a finite field to

guarantee each element has a unique inverse in the modulus operation. This also ensures

that each user has N different frequencies for N continuous time slots, which utilizes the

full available FM bandwidth of the frequency hopping radar. Any pair of EHC codes

from the same EHC code set has cross-correlation $H_{xy} = H_{cm} = 1$. That is because the

first element is always a zero and there are no overlapping codes elsewhere. Therefore,

an EHC FH code system can accommodate $N-1$ users concurrently.

The implementation of an EHC code system is shown in Fig. 2.19. First of all,

choosing zero as the start value of the sequence for the initial condition in this case. In

addition, generating

$$g_i(k) \equiv i \cdot k \quad mod\ (p) \tag{2.10}$$

by using recursive addition to replace the multiplication operation defined as:

$$g_i(k+i) \equiv g_i(k) + i \quad mod(p). \tag{2.11}$$

This step reduces the computing complexity, which results in saving the computing

power and time especially when the number is big. Finally, applying multiplicative

inverse mapping to $g_i(k)$ in order to get the $y_i(k)$ as:

$$y_i(k) \equiv \left(g_i(k)\right)^{-1} \ mod(p). \tag{2.12}$$

where the multiplicative inverse is defined as:

$$\left(g_i(k)\right)^{-1} \cdot g_i(k) \equiv 1 \ mod(p). \tag{2.13}$$
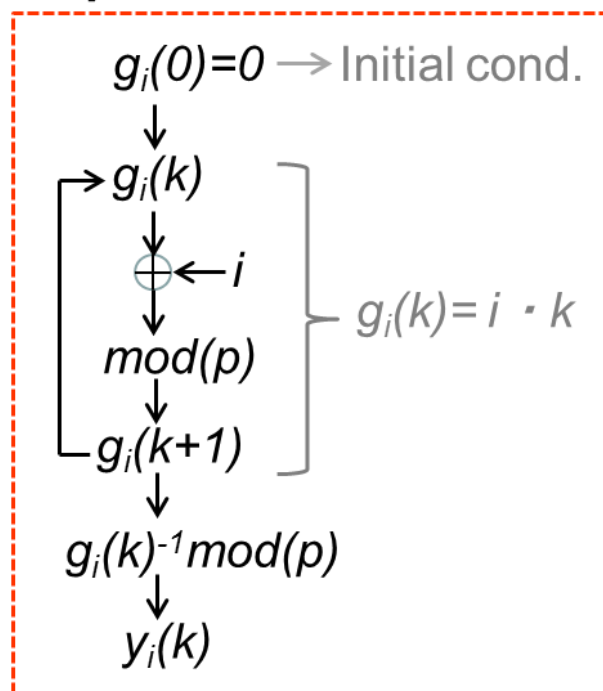
Implementation:

Fig. 2.19 Implementation of the EHC code.

40

Using N = 5 for example to create an EHC code set as follows:

$$User\ (i = 1): \{\ 0, 1, 3, 2, 4\ \} \tag{2.14}$$

$$User\ (i = 2): \{\ 0, 3, 4, 1, 2\ \}$$

$$User\ (i = 3): \{\ 0, 2, 1, 4, 3\ \}$$

$$User\ (i = 4): \{\ 0, 4, 2, 3, 1\ \}$$

which means user i = 1 (U_1) has the frequency sequence {f_0, f_1, f_3, f_2, f_4} to hop with

time and so on. Fig. 2.20 shows the Hamming correlation property of this EHC code set.

The x-axis is user id i, y-axis is the circular time shift τ , and z-axis is the magnitude of

Hamming correlation $H_{xy}(\tau$). If we choose user $i = 4$ (U_4) as the reference (REF), other

users i = 1, 2, 3 (U_1, U_2, U_3) are interference (INT). When reference signal correlates

with itself, resulting in an auto-correlation function, it has a peak of five at zero delay

and is zero elsewhere. When reference signal correlates with interference, resulting in

an cross-correlation function, it has the maximum level of one for all delays. That is,

(H_{am}, H_{cm}) = (0, 1), fulfills one-coincident FH code. When all four user signals sum

together, the total interference level becomes $H_{xy}(\tau) = (N - 1) - 1 = 3$, $\tau \neq 0$. The signal

peak is $H_{xy}(0) = N = 5$. Therefore, the target signal can be extracted from the

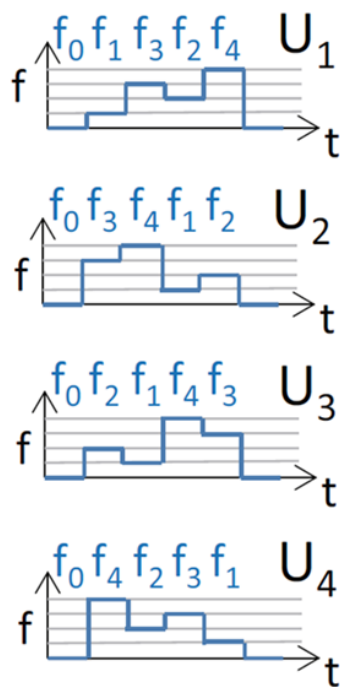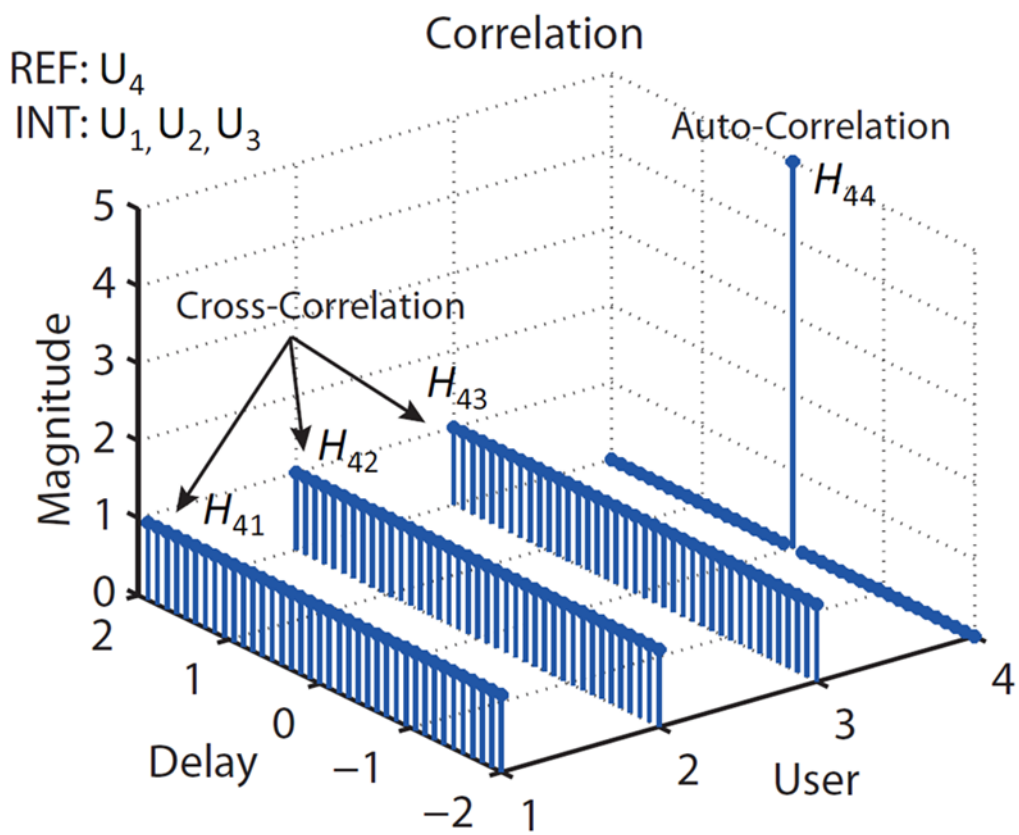interference in the multi-user environment.

41

(a)

(b)

Fig. 2.20 Correlation property of an EHC code set with $p = 5$.

Chapter 3

Implementation and Measurement

3.1   Implementation

Fig. 3.1 shows the implemented FH radar system block diagram. The FH waveform generator captures the EHC codes and outputs the EHC FH waveform to transmitter and delay unit. The receiving signal is correlated with the delayed version of the reference signal for further DSP operation. The algorithm controls EHC code generator, delay, and DSP to estimate the range and velocity of vehicles. The transmitter (TX), receiver (RX), and waveform generator are calibrated through the tuning digital-to-analog converters (DACs), which control the biasing of the circuit blocks, to optimize the FH radar function.
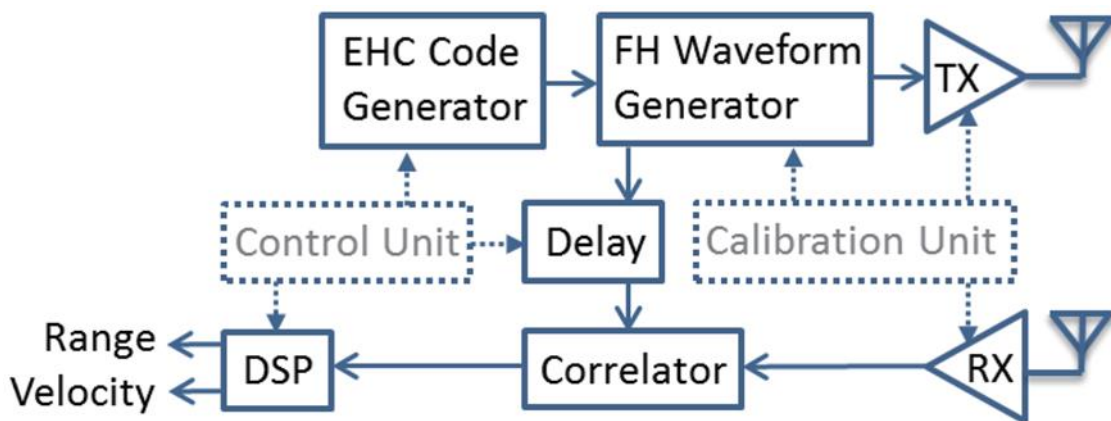
Fig. 3.1 Radar system block diagram.

3.1.1 Receiver

Fig. 3.2 shows the receiver architecture, including an input low-noise amplifier (LNA), transconductor (Gm) stage, passive mixer, lowpass filter (LPF), and the calibration DACs. The LNA amplifies the RF signal and the Gm stage converts this voltage signal to current mode. The current signal flows through a passive mixer and is filtered by the LPF.
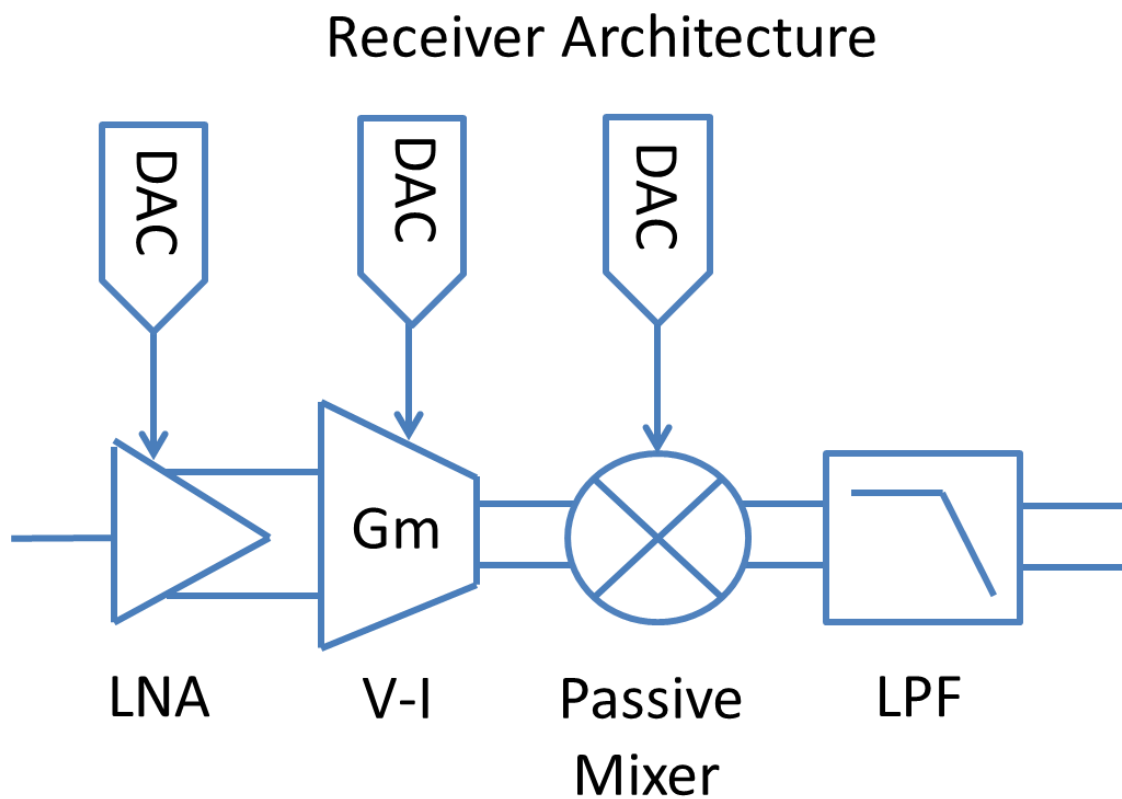

Fig. 3.2 Receiver architecture.

Fig. 3.3 shows the schematic of the LNA. This LNA is a transformer-coupled single-stage differential common-source (CS) amplifier with neutralization capacitors. The first transformer is used as a balun that converts the single-ended RF signal to differential. The cross-coupled neutralization capacitors match the feedback parasitic capacitance of the CS transistors to cancel out the feedback signals, which improves the stability so does the maximum stable gain of the CS amplifier. The output transformer provides the voltage gain for the following stage. The bias of the CS stage is controlled by the calibration DAC.
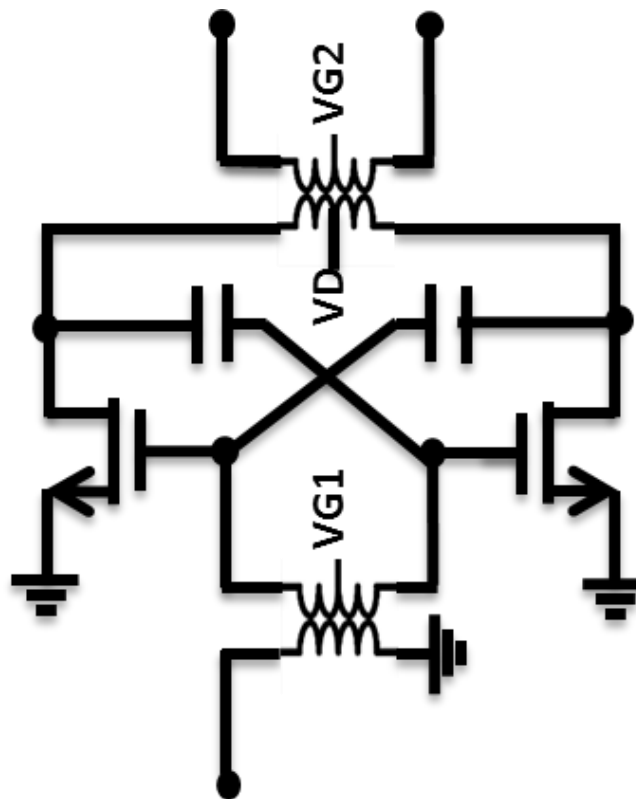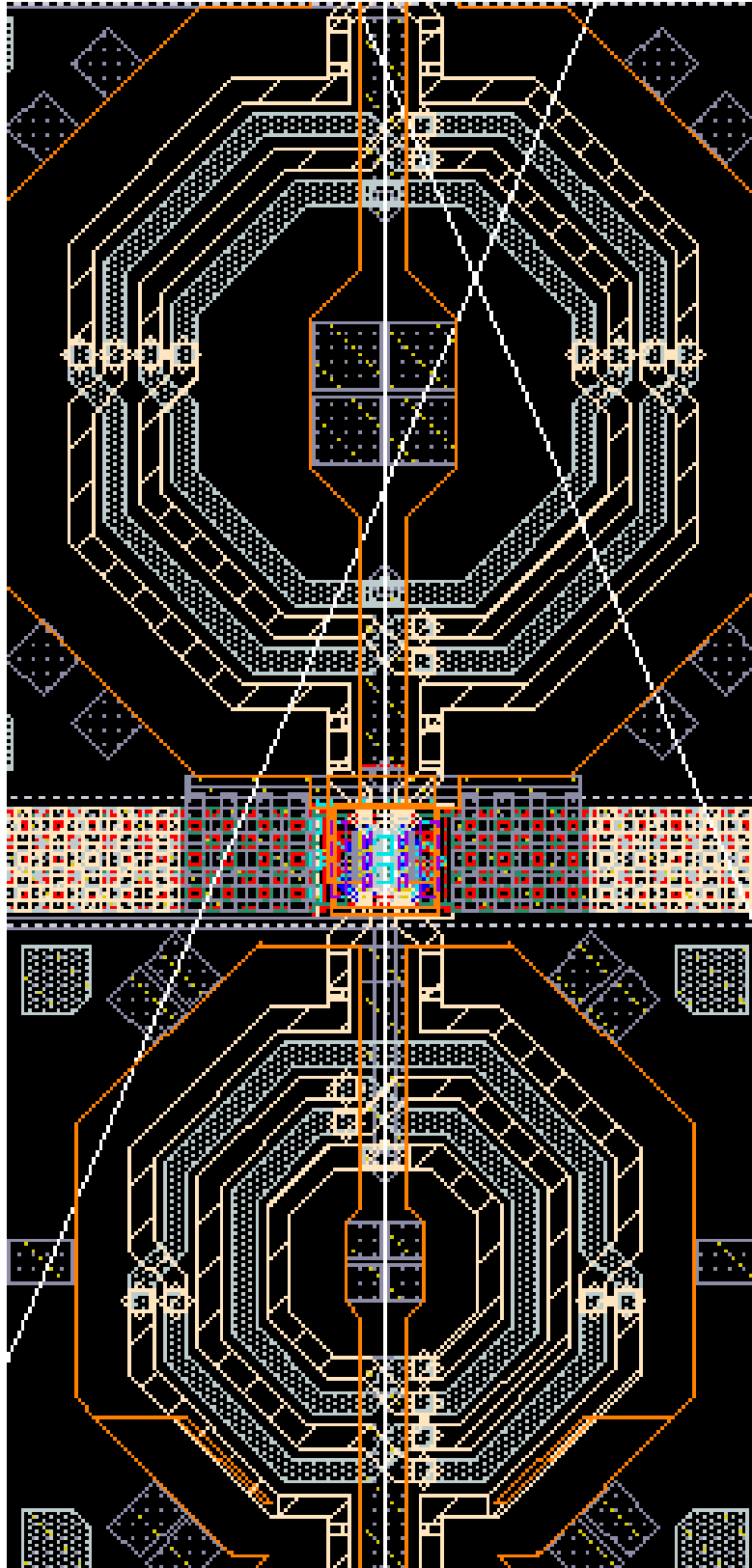

Fig. 3.3 LNA schematic.

Fig. 3.4 LNA layout.

Fig. 3.4 shows the layout of the LNA where the transformer is constructed by edge-coupled metals, which has balanced performance, low loss, and good coupling factor.

Fig. 3.5 shows the schematic of the Gm stage. This Gm stage converts the voltage signal to current signal with neutralization capacitors to improve the stability and stable gain. The output transformer provides the current gain for the current-mode operation of
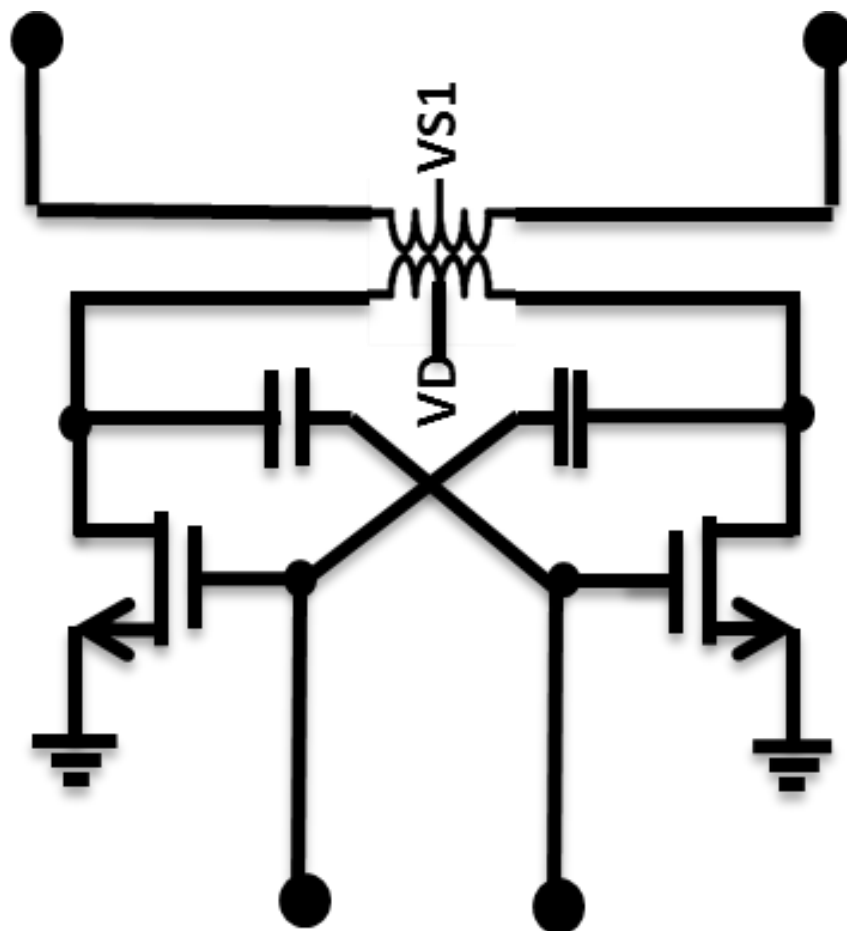

Fig. 3.5 Gm stage schematic.

the following stage. Fig. 3.6 shows the schematic of the passive mixer and the lowpass

filter. This passive mixer operates in current mode to improve the linearity of the

receiver, and the output capacitor filters out the high frequency components after mixing

operation. Fig. 3.7 shows the combined layout of the both Gm stage and the mixer. The

transformer has 3:2 ratio to boost the current signal from the Gm stage and input to the
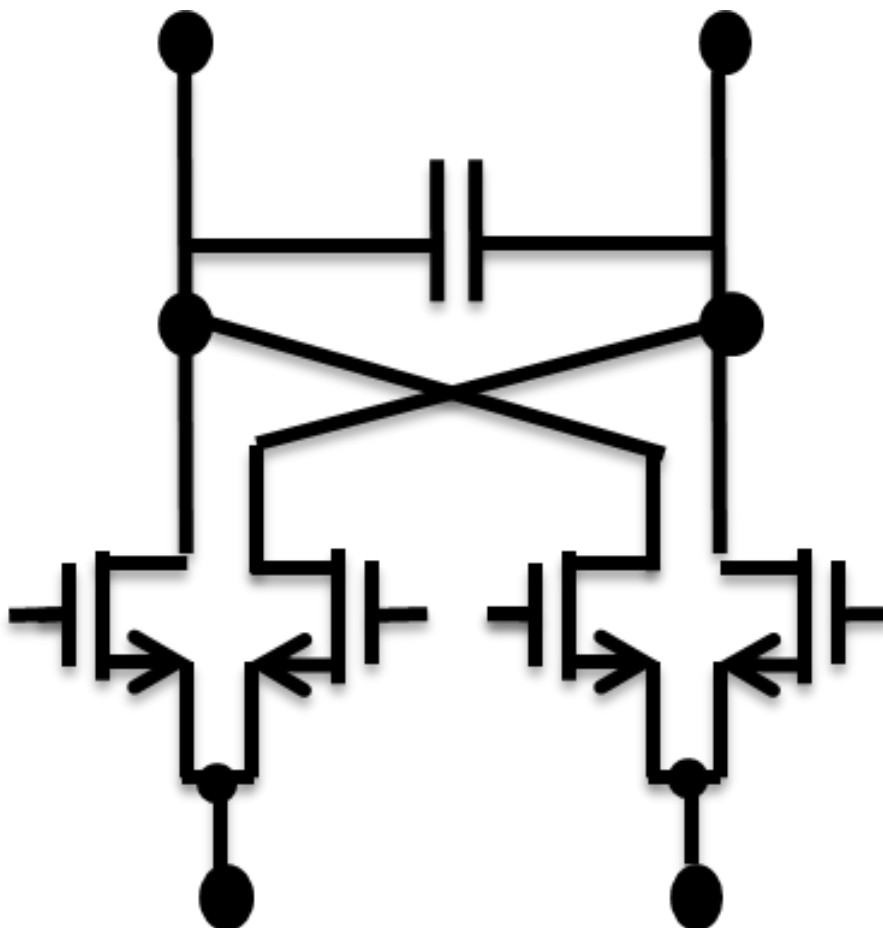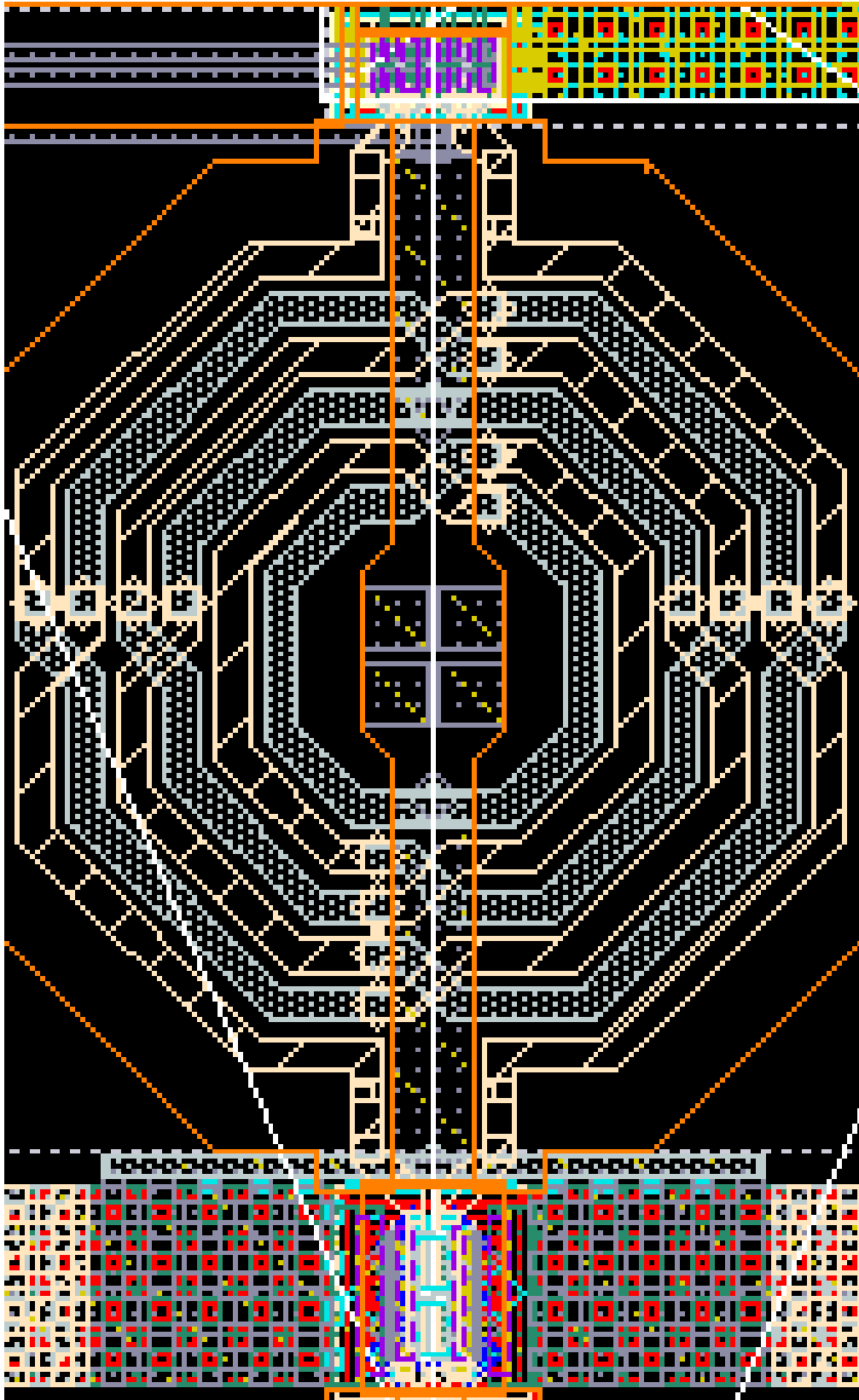
mixer.

Fig. 3.6 Schematic of mixer and LPF.

Fig. 3.7 Layout of Gm stage and mixer.

Fig. 3.8 shows the simulation results of the receiver. The maximum conversion gain is 31.5dB in high-gain mode and is 27dB in low-gain mode both with the 3-dB bandwidth around 2GHz shown in Fig. 3.8 (a). This also demonstrates the capability of the calibration for the receiver conversion gain, which has accomplished by the DACs. Fig. 3.8 (b) shows the noise figure (NF) of the receiver. The minimum NF is 4.2dB and it has similar NF performance in both gain modes. Fig. 3.8 (c) shows the S11 of the receiver. The S11 is lower than -10dB for the usable bandwidth in high-gain mode and shifts to higher frequency in low-gain mode. Fig. 3.8 (d) shows the linearity of the receiver. The input 1-dB compression point (P_{1dB}) is -40dBm in high-gain mode and goes up to -37.5dBm in low-gain mode.
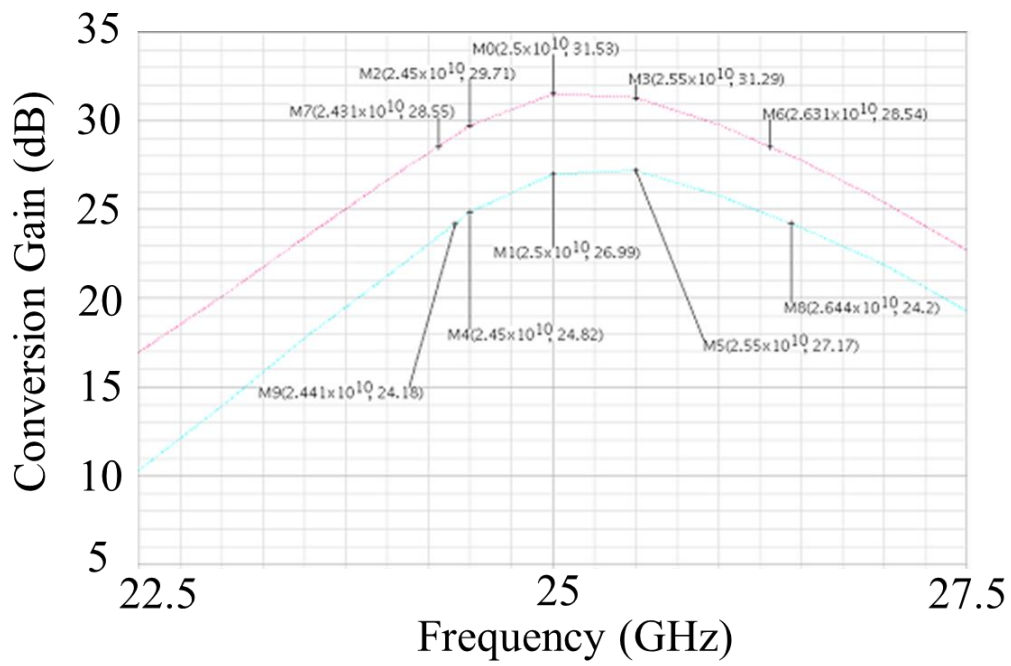
Fig. 3.8 (a) Receiver simulation results: conversion gain.
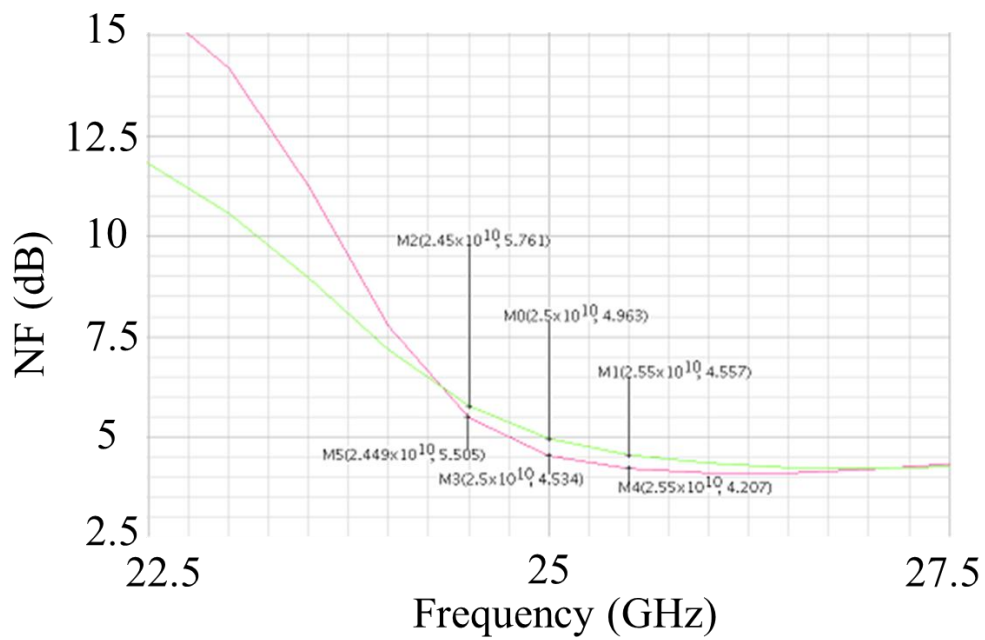
Fig. 3.8 (b) Receiver simulation results: noise figure.
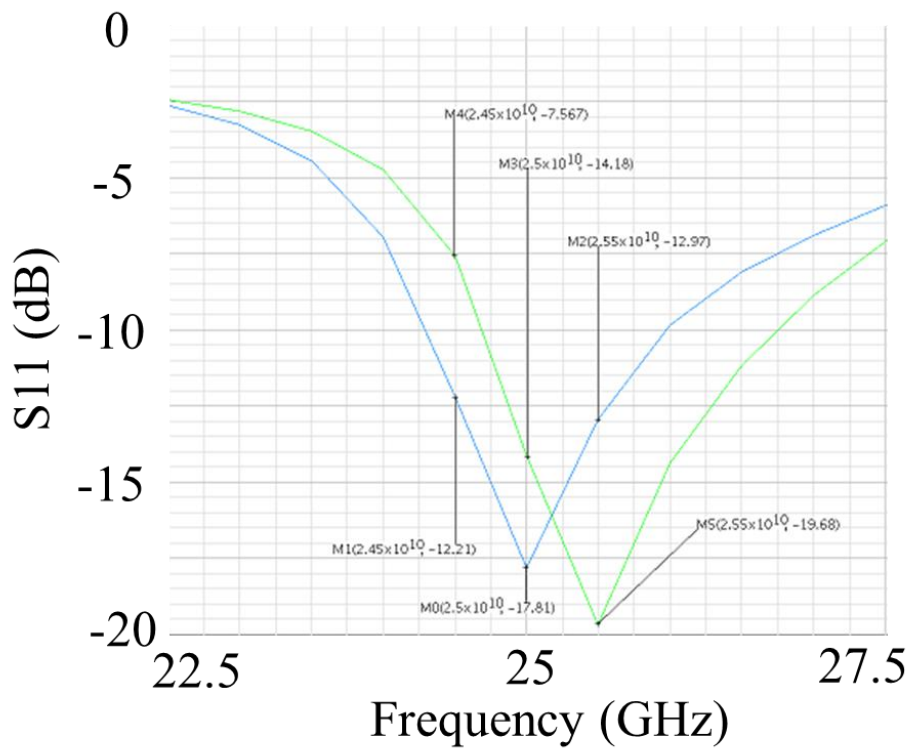
Fig. 3.8 (c) Receiver simulation results: S11.
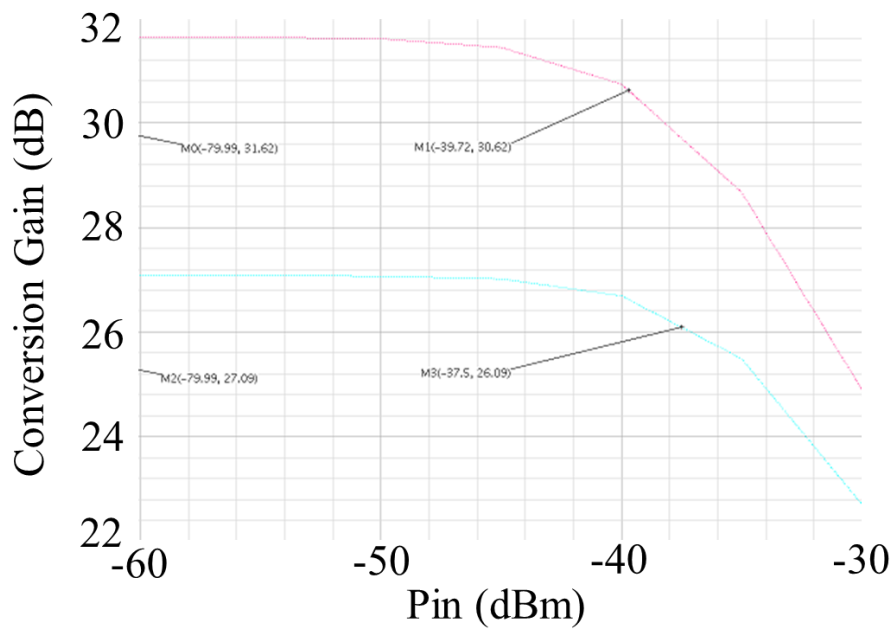
Fig. 3.8 (d) Receiver simulation results: linearity.

3.1.2　　　Power Amplifier

Fig. 3.9 shows the architecture of the power amplifier where pre-driver provides the gain to drive the main PA and the main PA provides the power to drive the load. This main PA also has the function of differential to single-ended convertor to output the RF signal. The bias of both pre-driver and main PA is controlled by the calibration DACs.
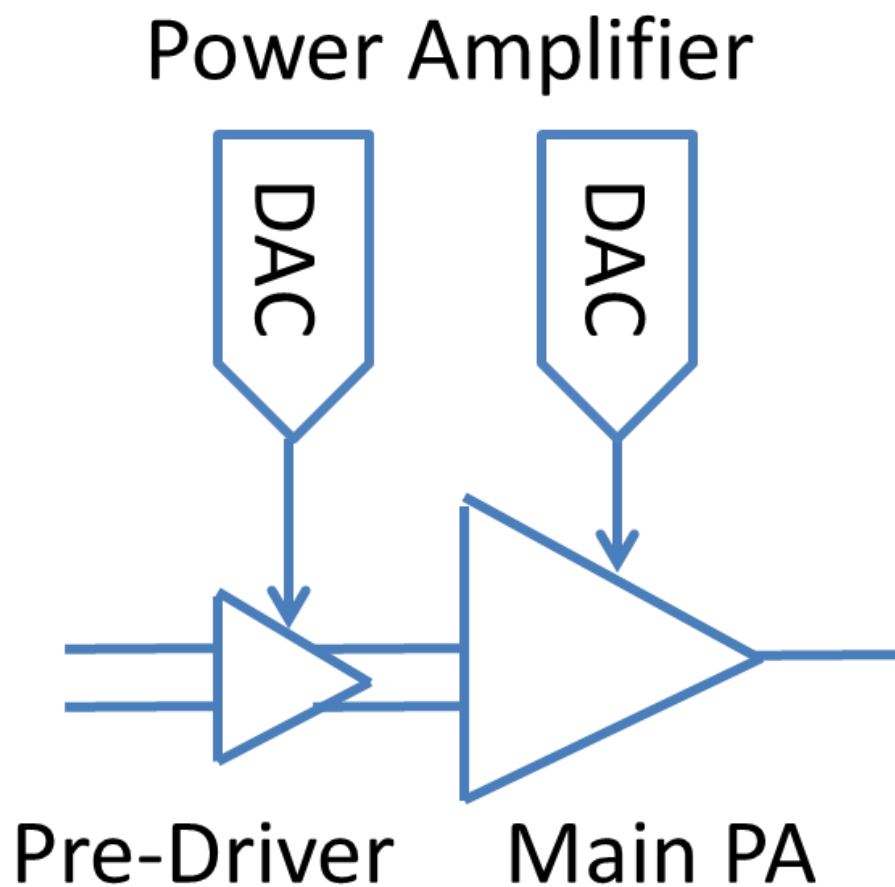
Fig. 3.9 Power amplifier architecture.
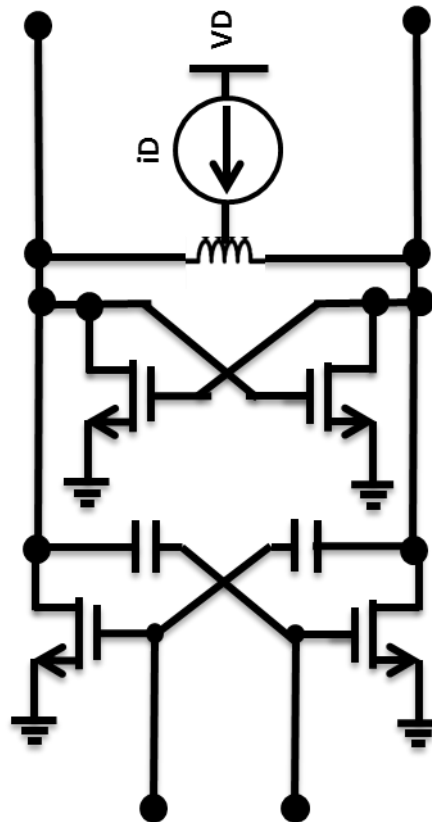
Fig. 3.10 Pre-driver schematic.

Fig. 3.10 shows the schematic of the pre-diver. This pre-driver is a CS amplifier with neutralization capacitor to improve both stability and stable gain. The additional cross-coupled transistors at the load provide the negative-gm to cancel some portion of the parasitic resistance in the load inductor, which minimizes the conductor loss of the inductor. The strength of the negative-gm can be controlled by the bias current source, which results in the gain change of the pre-driver. Fig. 3.11 shows the layout of this pre-driver.
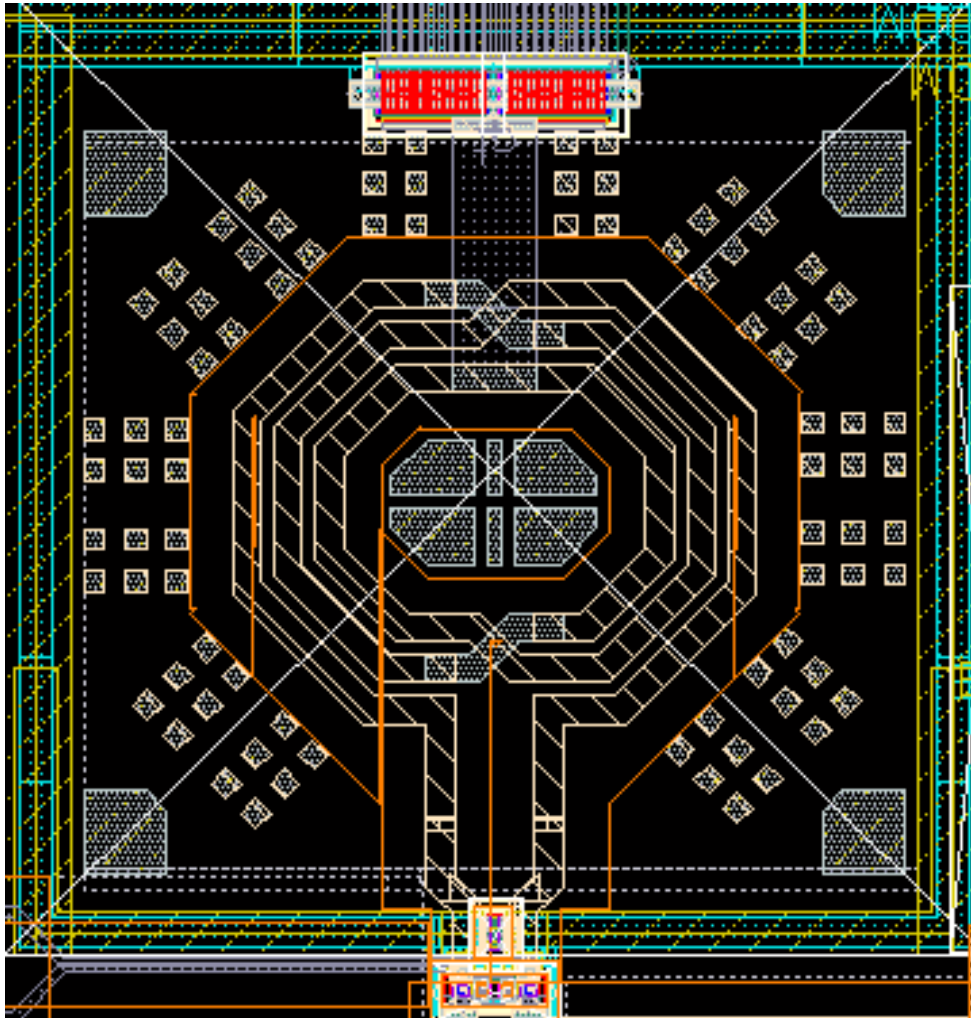
Fig. 3.11   Pre-driver layout.

Fig. 3.12 shows the schematic of the main PA. It is also a CS amplifier with neutralization capacitor to improve the stability and the stable gain. The main PA transistors are much bigger than the pre-driver to provide enough driving capability for the load. The output transformer is used for the purpose of impedance transformation in order to achieve the best power matching.
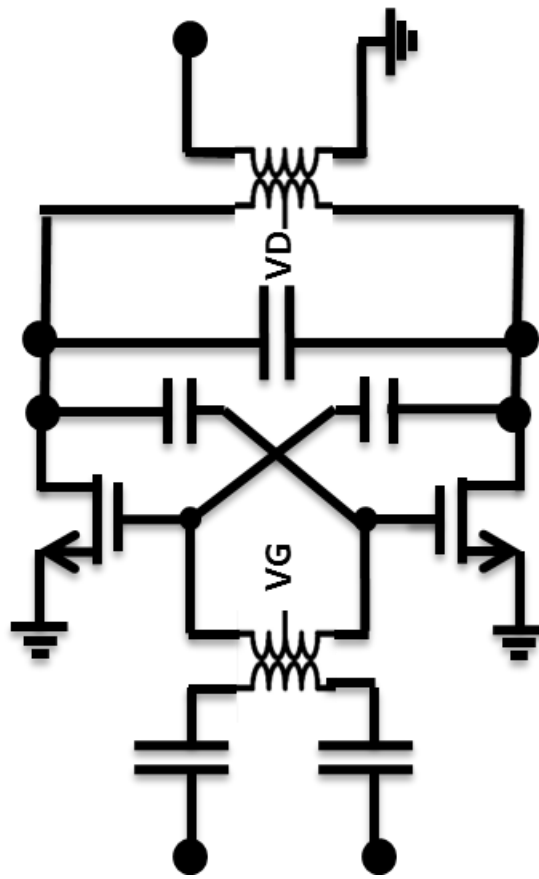
Fig. 3.12 Main PA schematic.

The output capacitor is added to resonate the inductance of the output transformer at the desired frequency. On the input side, there is also a transformer for the impedance transformation, which provides the power matching at the source to further extend the driving capability. The input capacitors are also added to resonate the inductance of the transformer at desired frequency. Fig. 3.13 shows the layout of the main PA. The metal width of the output transformer is enlarged to accommodate the high current of the main PA.
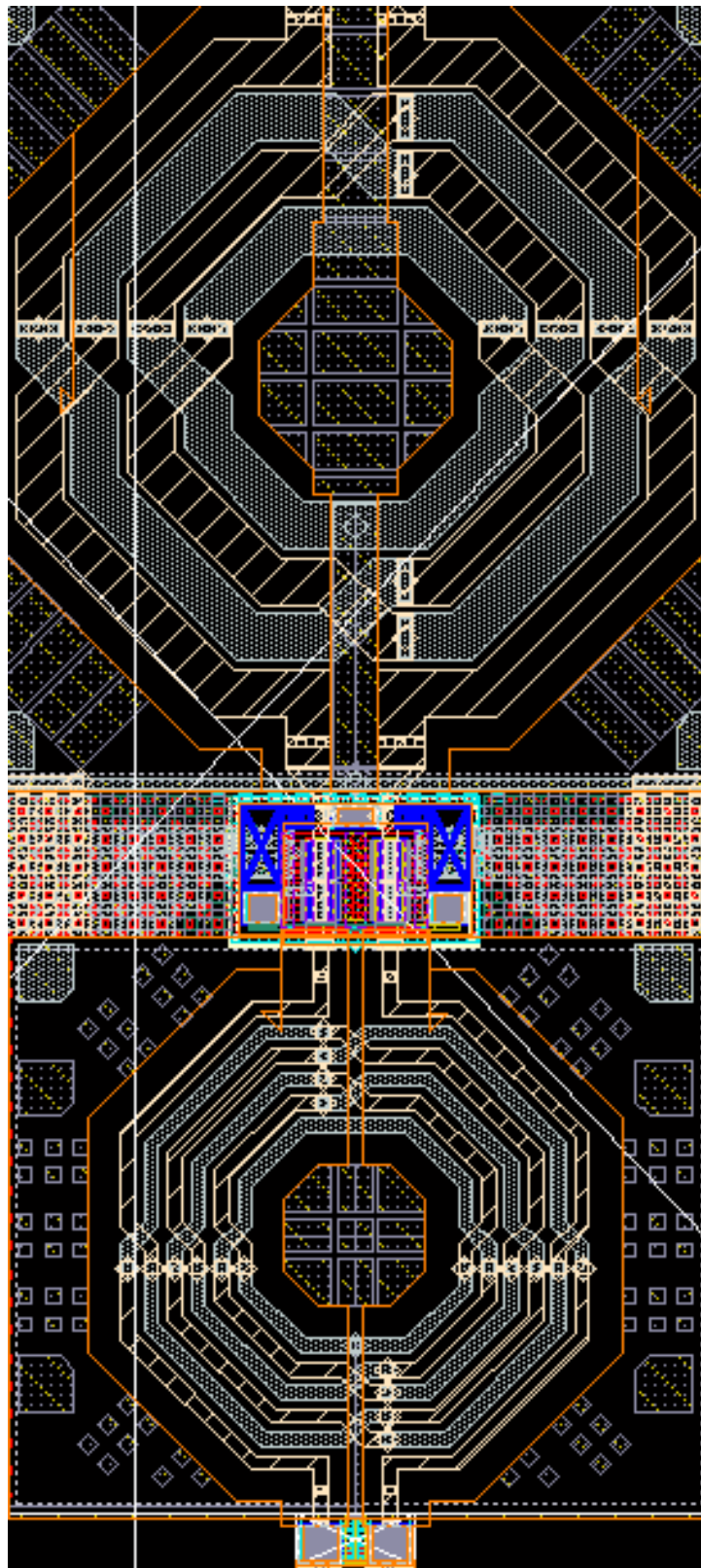
Fig. 3.13 Main PA layout.

Fig. 3.14 shows the simulation results of the power amplifier. The maximum power gain is 10dB in high-gain mode and down to 6dB in low-gain mode shown in Fig. 3.14 (a), which demonstrates the capability of the PA gain tuning by the calibration DACs. The 3-dB bandwidth is around 3.3GHz that is wide enough to cover the entire usable bandwidth in both high-gain and low-gain modes. Fig. 3.14 (b) shows the linearity of the PA with left y-axis as gain and right y-axis as output power (P_{out}). The output P_{1dB} is 6.4dBm and the saturation power level is 11.5 dBm. Fig. 3.14 (c) shows the S11 of the PA. The S11 is better than -10dB for the entire usable bandwidth.
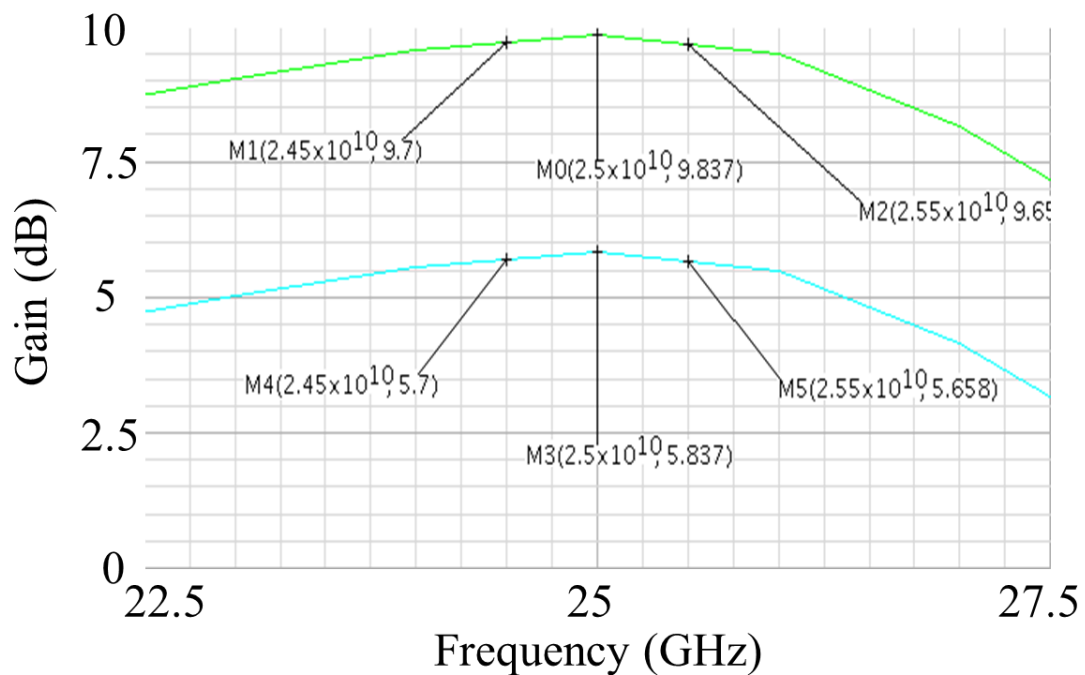
Fig. 3.14 (a) Power amplifier simulation results: power gain.
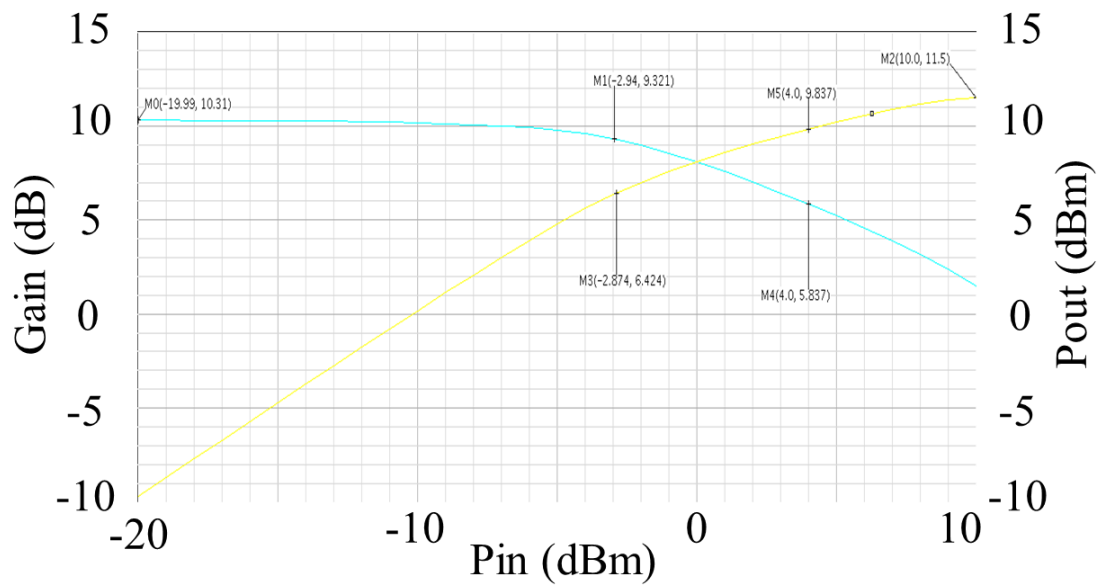
Fig. 3.14 (b) Power amplifier simulation results: linearity.
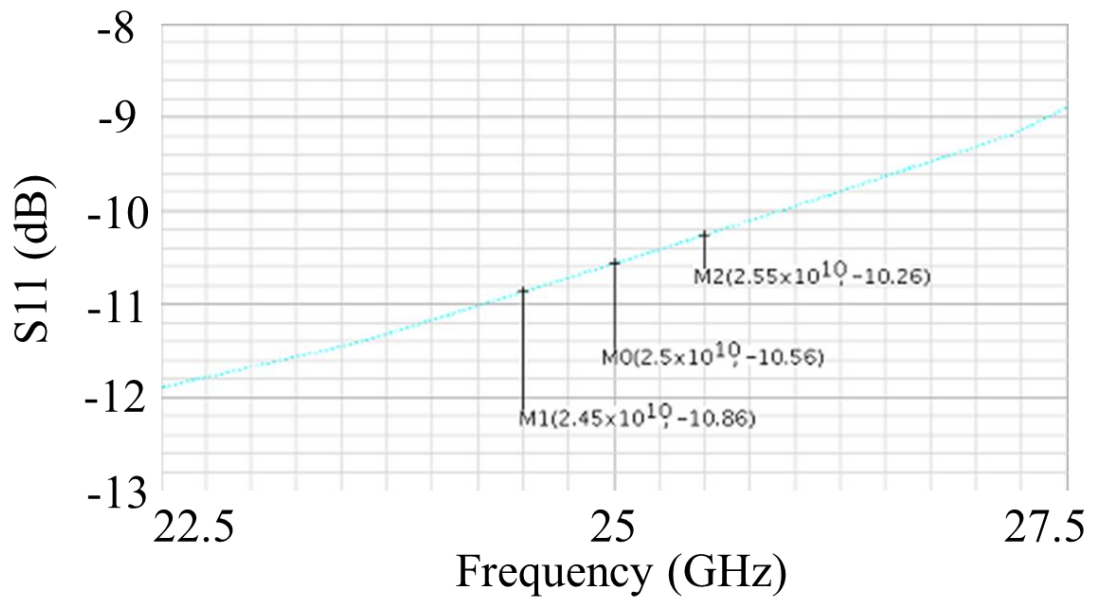
Fig. 3.14 (c) Power amplifier simulation results: S11.

59

3.1.3   Radar Platform

Fig. 3.15 shows the implemented FH radar measurement platform. EHC code generator produces the encoded EHC data and clock to the radar module. The data receiver, serial-to-parallel demux, and mapping decoder are integrated on chip to drive a FH waveform generator. The total bandwidth of the FH signal is 1GHz with 8-bit frequency step resolution. The on-chip TX radiates at 24GHz through the horn antenna. The RX horn antenna receives the reflected signal from the metal plate target placed 2m away. The down-converted baseband signals are captured by oscilloscope for further post processing on PC.

Fig. 3.16 shows the microwave radar module. This microwave module is 8cm by 4cm including the connectors, which carries the 24GHz signals, analog baseband
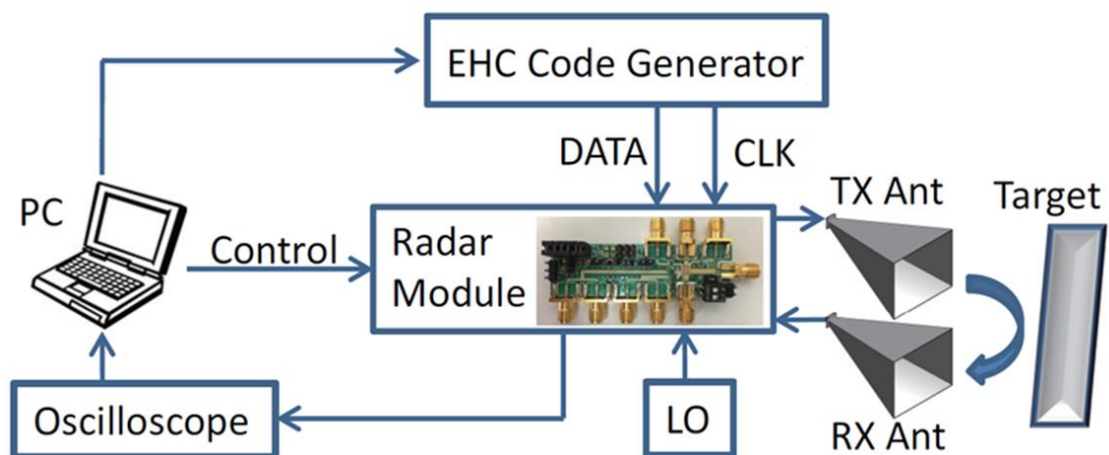
Fig. 3.15 Radar platform setup.

signals, and high-speed digital signaling. The 24GHz signals run at top (TX), bottom (RX), and right (LO), and each signal is connected through a dedicated high frequency SMA connector that can work up to 26.5GHz. The baseband signals go to bottom (BB) running with differential to minimized the coupling from other signals. The high-speed digital signals come from top (DATA and CLK) running with lowest amplitude to maintain the signal quality as well as minimize the interference to other signals. The test pins monitoring the signals are build at the bottom right corner with a switch to manually debug the DATA and CLK. The digital control interface is build with a header (Control) to control the function of the CMOS chip. The radar IC fabricated by 65nm CMOS includes frequency hopping generator, digital control serial interface, RF transceiver, and calibration circuitry.
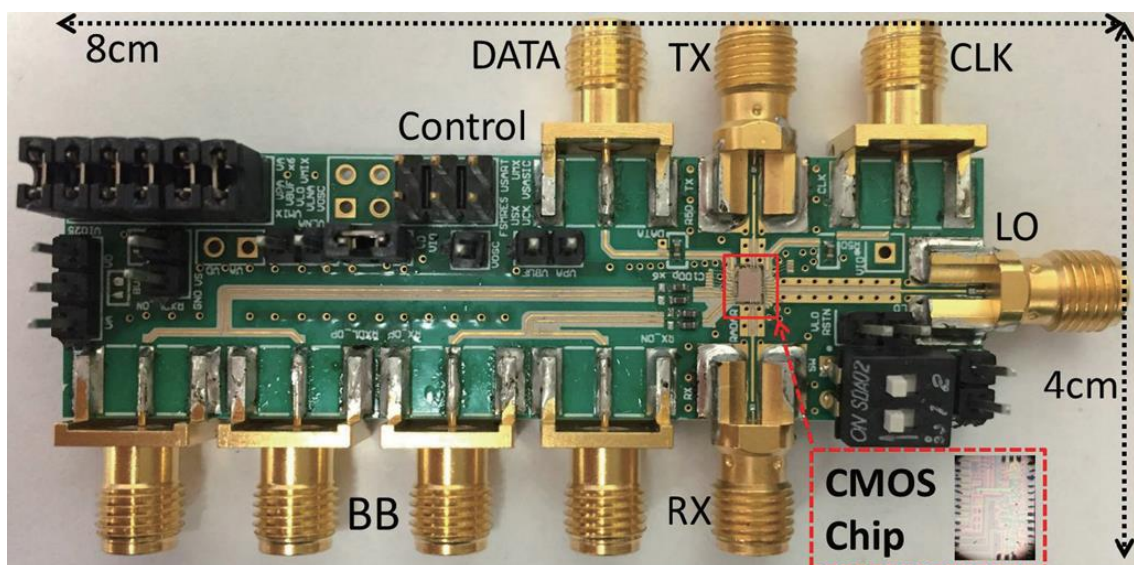
Fig. 3.16 Microwave radar module and CMOS chip.

In order to get the 24GHz out from the printed circuit board (PCB), the assembly is the major issue to deal with shown in Fig. 3.17. This PCB combines two types of different substrates, which includes the Rogers (RO) microwave substrate on the top and the commercial FR4 low-cost substrate for the electrical power supplies as well as the mechanical support shown in Fig. 3.17 (a). The low loss tangent RO substrate carries the microwave signals with low dielectric loss and good integrity. Moreover, choosing high dielectric constant minimizes the dimension of the transmission lines smoothing the transition between the chip and the board. The RO substrate is milled down by the depth equal to the thickness of the CMOS chip, which minimizes the bondwire connections as well as their parasitics.
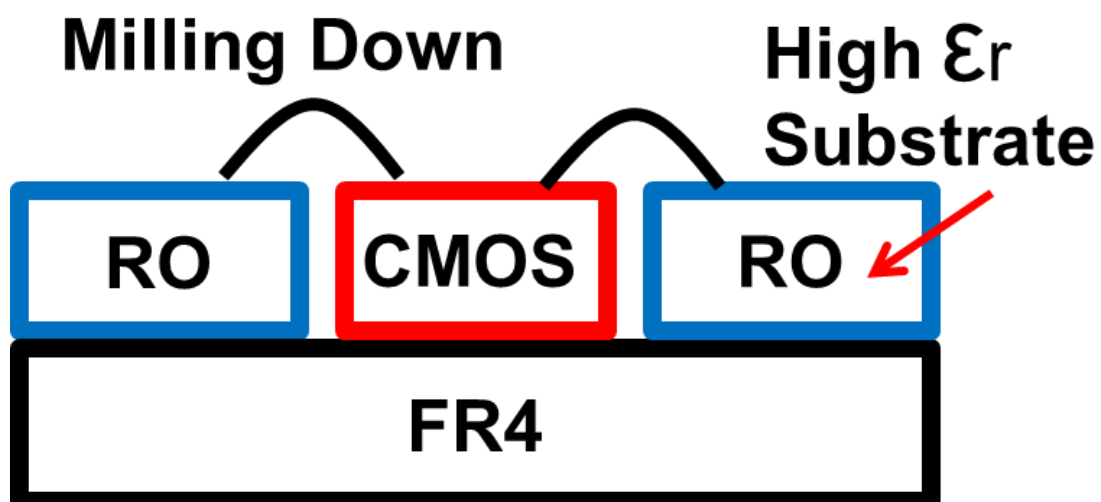
Fig. 3.17 (a) Assembly: Rogers with FR4

Milling Down
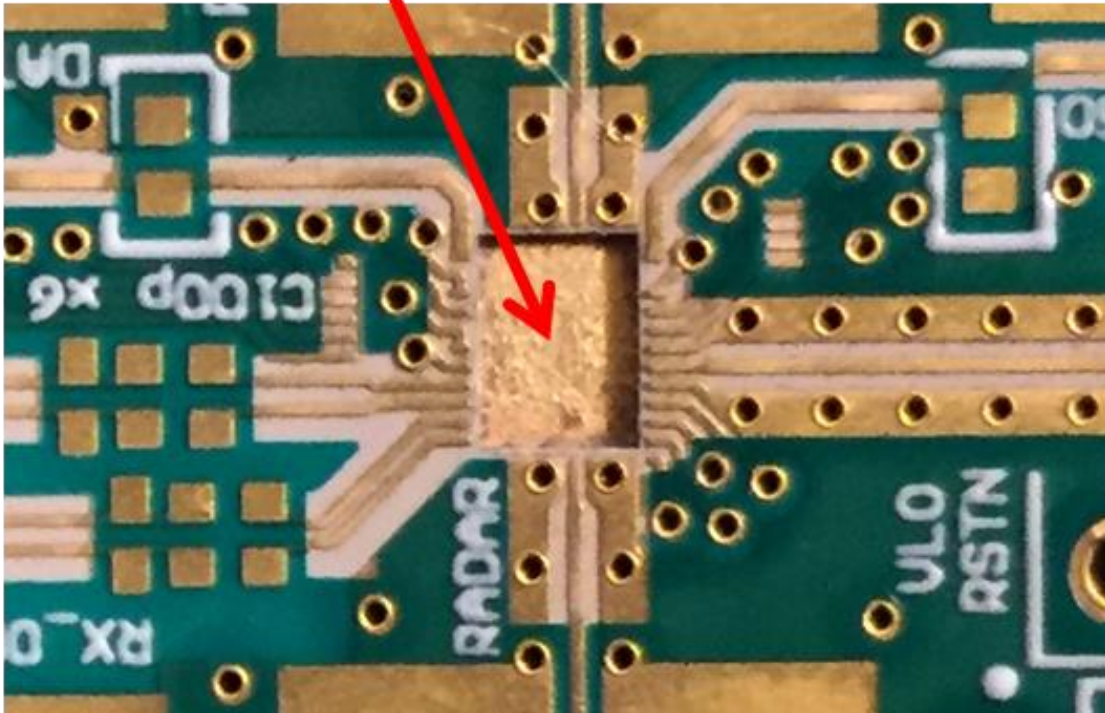
Fig. 3.17 (b) Assembly: milling down space.

The milling down space shown in Fig. 3.17 (b) has the ground plane to dissipate the heat. All the 24GHz signals are carried by the coplanar waveguide (CPW) shown in Fig. 3.17 (c) to isolate the microwave signals from other signal sources. The ground vias of the CPW have to close to the chip as much as possible to maintain the electrical property of the CPW at microwave frequency. The spacing of the first two ground vias also needs to be minimized for better microwave grounding. Exposing the metal of the CPW to the air controls the impedance well at microwave frequency. The size of both
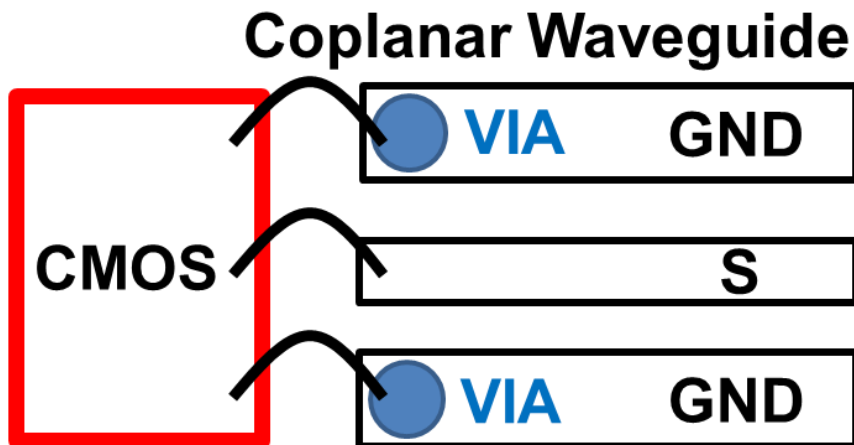
Fig. 3.17 (c) Assembly: CPW ground vias.

bonding pads on the chip and on the board are enlarged to accommodate double

bondwire on each pad to further reduce the parasitic inductance by half shown in Fig.

3.17 (d).
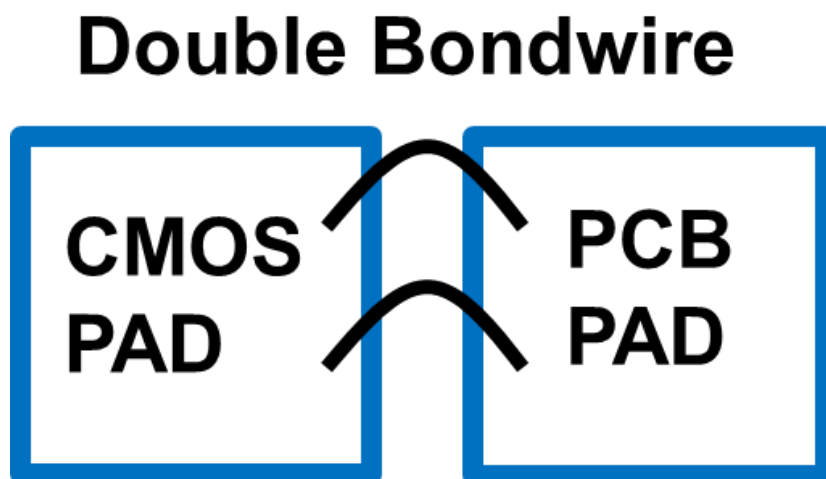
Fig. 3.17 (d) Assembly: double bondwire.

The radar system parameters are summarized in Table 3.1. The carrier frequency is 24GHz with FM bandwidth of 1GHz corresponding to 15cm resolution. The number of frequency step is 23 for 22 users, and the signal length is chosen so that the maximum unambiguous range is long enough for mid-range automotive radar operation. The measured transmit power is 4dBm and the measured NF is 9dB with the receiver gain of 22dB. These parameters are the overall system performance measured from the output of the connectors. That is, the transmit power, conversion gain, and noise figure include all the assembly and transition loss from the bondwires, traces, and connectors. The bandwidth of the system also counts in the parasitics of the assembly other than the chip itself.

Parameter	Value
Frequency	24GHz
Frequency Steps	23
Bandwidth	1 GHz
Frequency Steps	23
Symbol Rate	45 MHz
EHC Code Length	0.5 us
Number of Users	22
Resolution	15 cm
Maximum Unambiguous Range	75 m
Transmit Power	4 dBm
Receiver Conversion Gain	22 dB
Receiver Noise Figure	9 dB
Sideband Rejection	-30 dBc@ 500 MHz
Power Consumption	143 mW

Table 3.1 Summary of FH Radar System Parameters

3.2 Measurement Results

Fig. 3.18 shows the TX output spectrum of EHC FH radar at 24GHz. The bandwidth of the FH signal is 1GHz with the sideband rejection of 30dBc at 500MHz offset, which is the primary inherited advantage of the FH signal. There is no need for sideband cancellation technique in direct sequence SS radars shown in Fig. 3.19 [18].
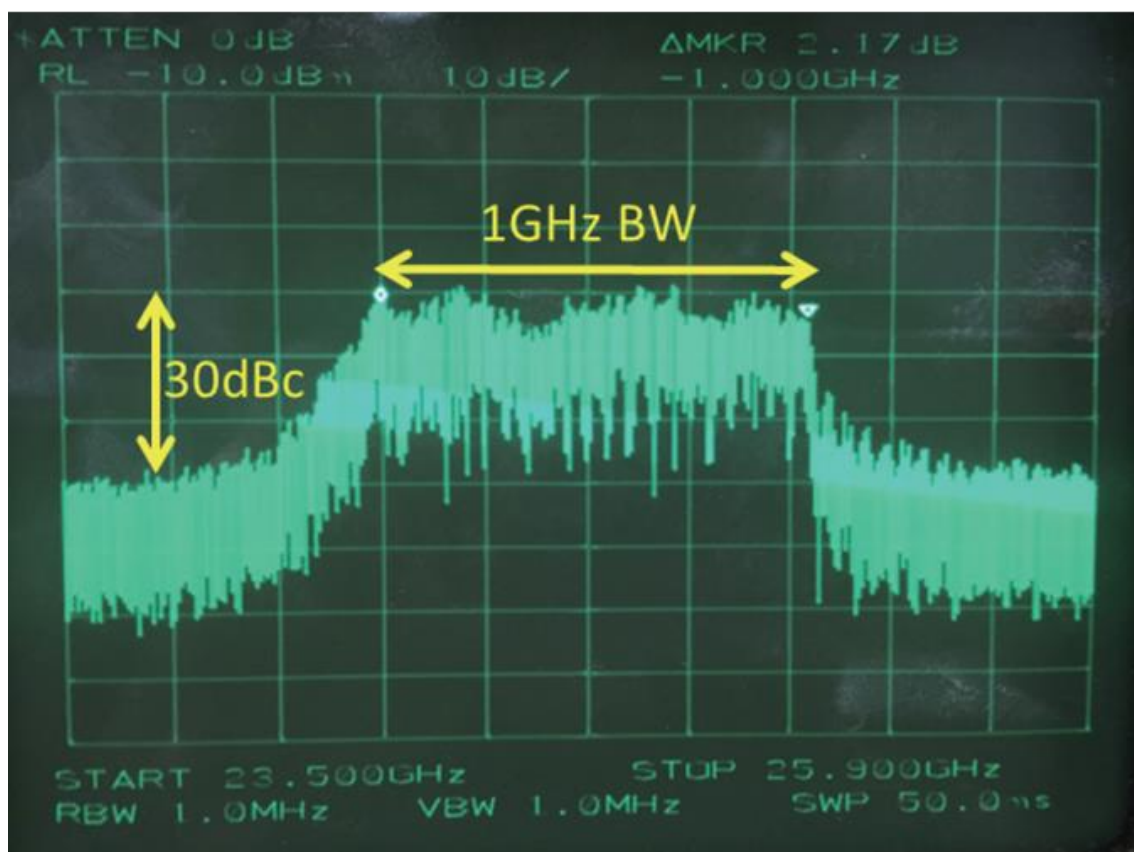
Fig. 3.18 EHC FH radar TX output spectrum at 24GHz.

DSSS Radar Spectrum
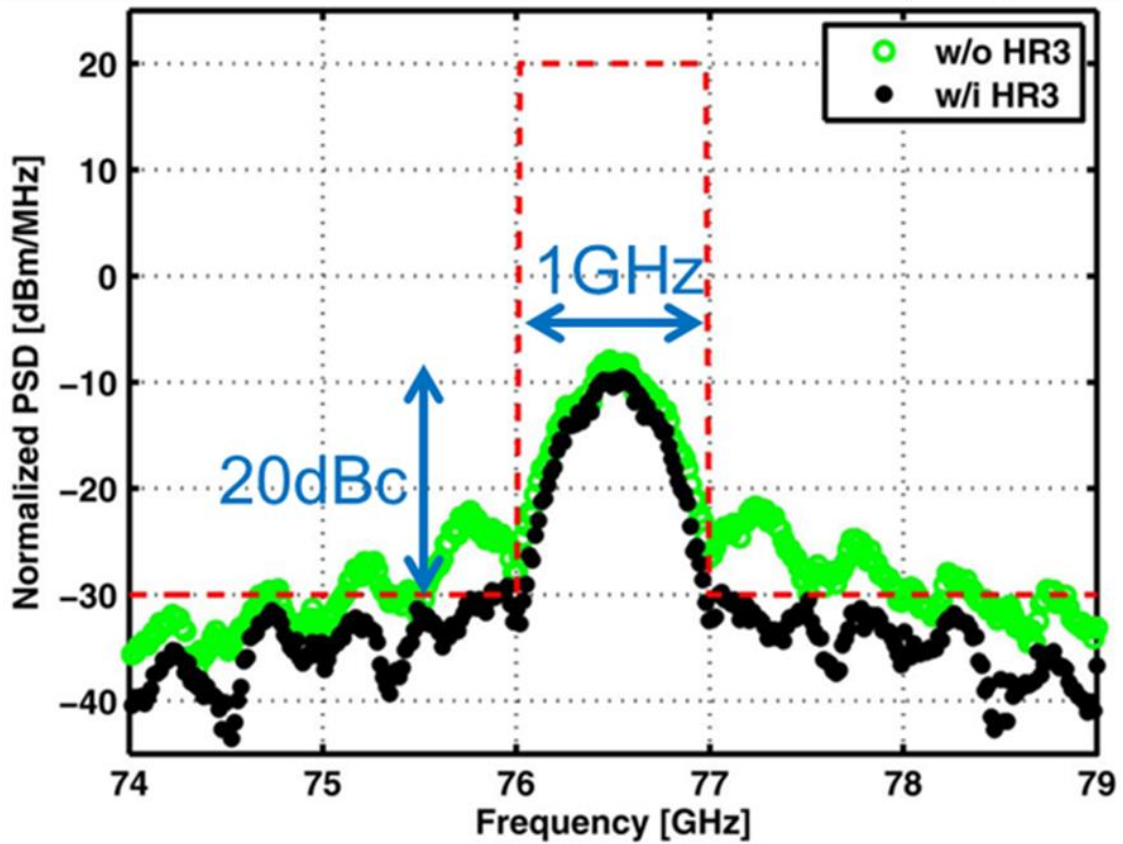
Fig. 3.19 DSSS Radar frequency spectrum.

In Fig. 3.19, the green curve is without sideband cancelation technique and the black curve has it. Without sideband cancellation technique, this DSSS radar only has 13dBc rejection due to the wideband code spreading. The sideband level goes down to 20dBc when applying special circuit and system technique. However, in FHSS radar, it is very easy to get 30dBc rejection due to the narrow bandwidth of frequency hopping at each sub-band.
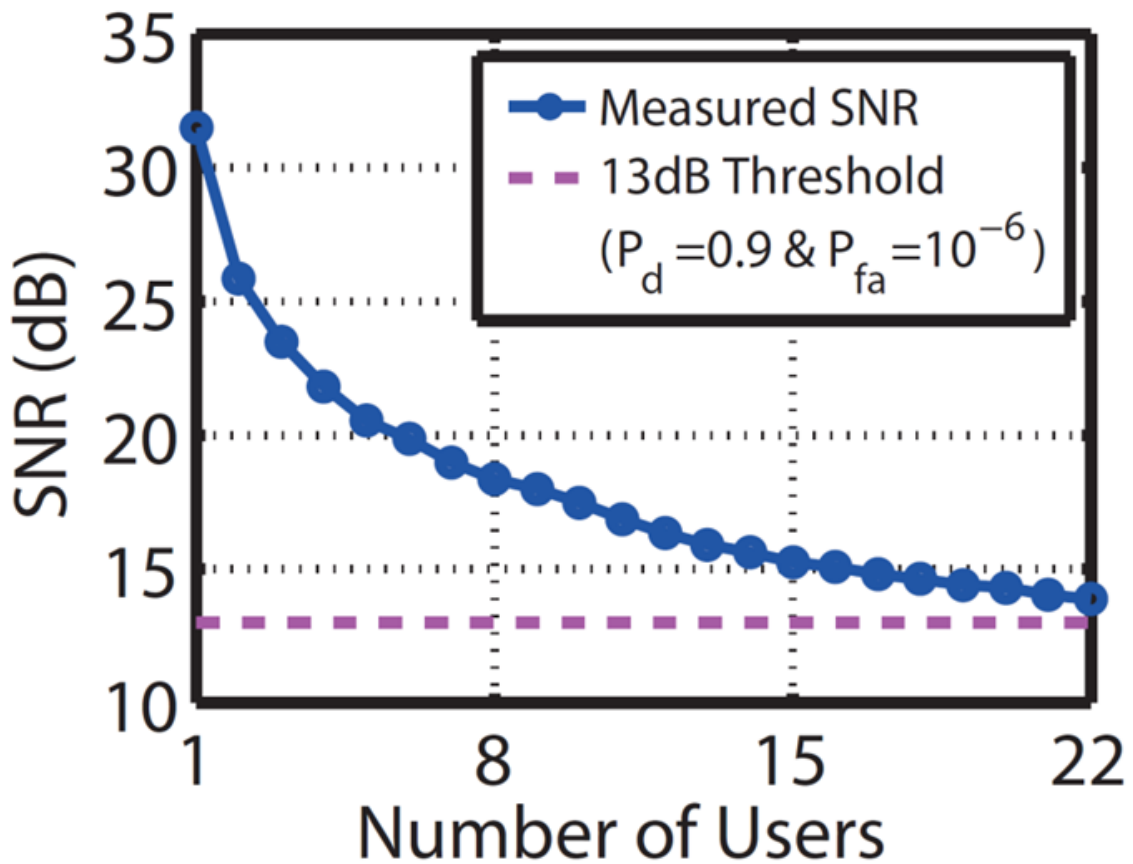
Fig. 3.20 Measured radar SNR in multi-user environment.

Fig. 3.20 shows the signal-to-noise (SNR) versus the number of users. The SNR decreases due to the increase of radar users and corresponding interferences. Nevertheless, the SNR stays above 13dB (dashed line) to maintain the detection probability $P_d = 0.9$ with the false alarm rate $P_{fa} = 10^{-6}$ according to the radar cookbook, which shows the typical detection probability versus SNR in a radar system shown in Fig. 3.21 [19].

Typical Pd vs. SNR in Radar System
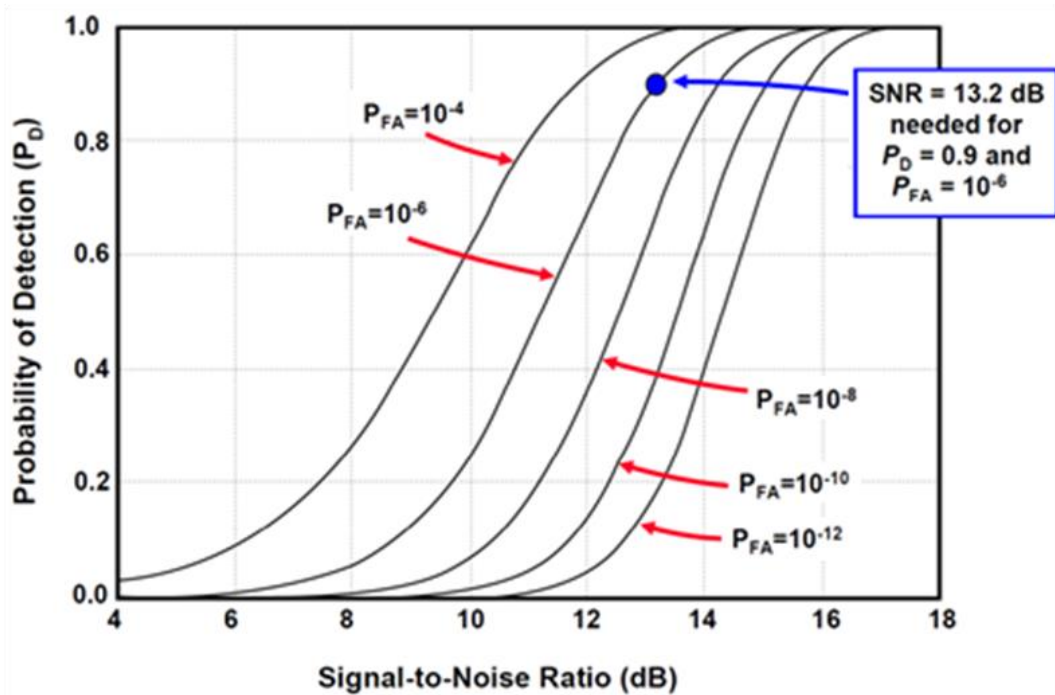
Fig. 3.21 Typical detection probability versus SNR in a radar system.

Fig. 3.22 shows the measured range plot of the EHC FH radar in multi-user environment. There are three different test scenarios. The first one is a single-user environment where reference correlates with the delay version of itself, which expresses an auto-correlation function. The red curve in Fig. 3.22 (a) is an auto-correlation function with a peak at 2m with average -32dB noise level normalized to the signal in a single-user environment. Obviously, the signal can be detected correctly in a single user scenario. The maximum unambiguous range of the radar is 75m due to the 0.5us code length.

Second is that the radar receives both target and interference together. In a 2-user

environment as the cyan curve shown in Fig. 3.22 (a), the average noise level goes up to

-25dB due to the interference introduced by the second user. The peak still appears at

2m with the average noise level of -14dB, which corresponds to the sum of all

interference from other 21 users. The blue curve in Fig. 3.22 (a) shows the reference

correlates with the sum of all 22 users, including the target. In fact, the overall average

noise level is actually the sum of the auto-correlation function and the cross-correlation

function.

In order to further verify the system, the last scenario shown in Fig. 3.22 (b) is that
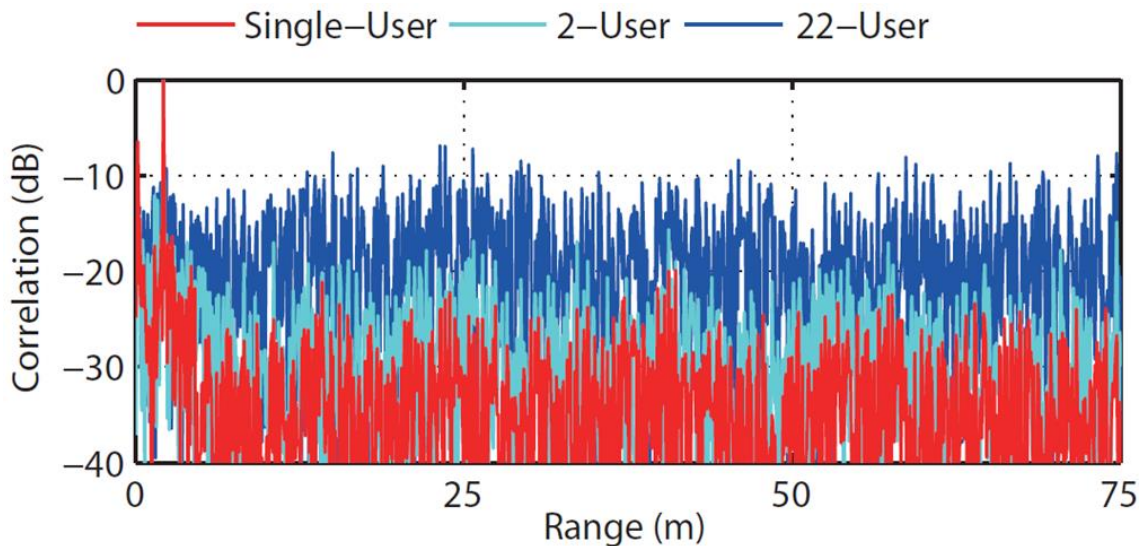
Fig. 3.22 (a) Measured range plot: auto-correlation in single-user (red) environment and

correlation in 2-user (cyan) and 22-user (blue) environment.

the radar receives only the interference from other users but no signals from the target. In this scenario, the reference signal correlates with other users that have different EHC codes, i.e., the cross-correlation function. The average interference level is around -26dB in a 2-user environment and -14dB in a 22-user environment, which matches to the results shown in Fig. 3.22 (a). Therefore, the result that the interference level is well-managed in EHC FH radar system has been verified. From these measurement results, this code-division FH radar can detect targets correctly in a multi-users scenario up to 22 of them. These results prove that EHC FH code has the needed interference immunity property for intended multi-user radar system.
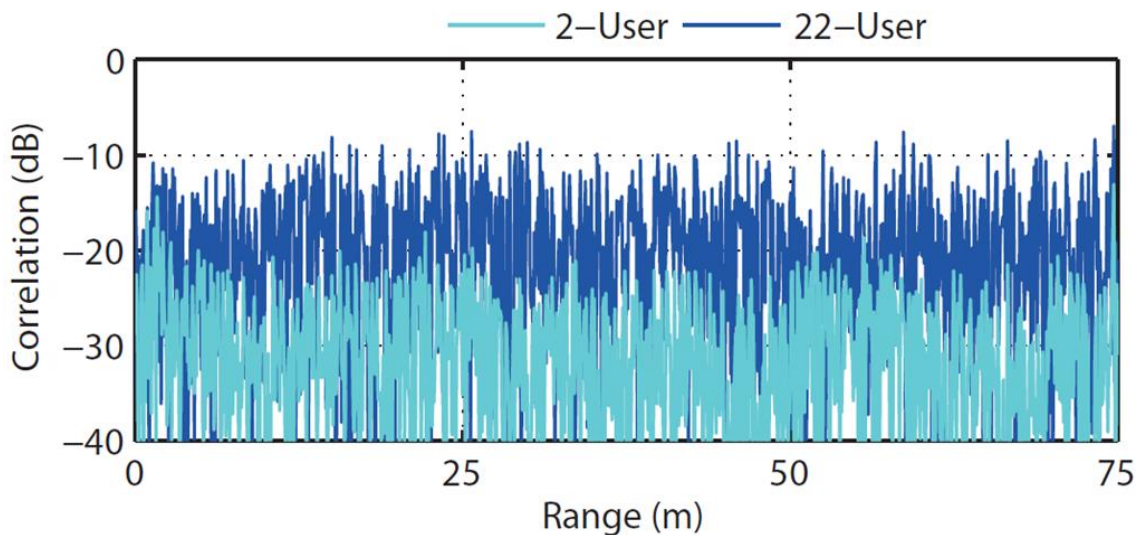
Fig. 3.22 (b) Measured range plot: cross-correlation in 2-user (cyan) and 22-user (blue) environment.

Chapter 4

Conclusions

In this dissertation, the potential radar interference issue for future multi-vehicle autonomous driving system has been addressed. An extended hyperbolic congruential (EHC) code as the one-coincidence frequency hopping (FH) code has been implemented in the CMOS radar prototype at 24GHz and its excellent performance has been validated. The interference level is well-managed in this EHC FH radar system with optimal Hamming correlation property.

An interference-tolerant multi-user radar system, based on the EHC FH code in a multi-vehicle environment for autonomous driving applications, has been realized. Up to 22 vehicles can co-operate at the same time/area with 1GHz bandwidth and with minimum 15cm range resolution.

References

[1]   "Look, No Hands," The Economist, Sep. 12, 2012.
       http://www.economist.com/node/21560989

[2]   Josie Garthwaite "Sharing the Road With Driverless Cars," Beacon, May 12,
       2014.
       https://www.beaconreader.com/climate-confidential/sharing-the-road-with-drive
       rless-cars

[3]   M. Steinhauer, H. O. Ruob, H. Irion and W. Menzel, "Millimeter-Wave-Radar
       Sensor Based on a Transceiver Array for Automotive Applications," *IEEE Trans.
       Microw. Theory Techn.*, vol. 56, no. 2, pp. 261-269, Feb. 2008.

[4]   S. T. Nicolson et al., "A Low-Voltage SiGe BiCMOS 77-GHz Automotive
       Radar Chipset," *IEEE Trans. Microw. Theory Techn.*, vol. 56, no. 5, pp.
       1092-1104, May 2008.

[5]   R. Feger, C. Wagner, S. Schuster, S. Scheiblhofer, H. Jager and A. Stelzer, "A
       77-GHz FMCW MIMO Radar Based on an SiGe Single-Chip Transceiver,"
       IEEE Trans. Microw. Theory Techn., vol. 57, no. 5, pp. 1020-1035, May 2009.

[6]   N. Pohl, T. Jaeschke and K. Aufinger, "An Ultra-Wideband 80 GHz FMCW
       Radar System Using a SiGe Bipolar Transceiver Chip Stabilized by a
       Fractional-N PLL Synthesizer," *IEEE Trans. Microw. Theory Techn.*, vol. 60, no.
       3, pp. 757-765, March 2012.

[7]   S. Trotta et al., "An RCP Packaged Transceiver Chipset for Automotive LRR
       and SRR Systems in SiGe BiCMOS Technology," *IEEE Trans. Microw. Theory
       Techn.*, vol. 60, no. 3, pp. 778-794, March 2012.

[8]   J. Hasch, E. Topak, R. Schnabel, T. Zwick, R. Weigel and C. Waldschmidt,
       "Millimeter-Wave Technology for Automotive Radar Sensors in the 77 GHz
       Frequency Band," *IEEE Trans. Microw. Theory Techn.*, vol. 60, no. 3, pp.
       845-860, March 2012.

[9]   J. Yu et al., "An X-Band Radar Transceiver MMIC with Bandwidth Reduction
       in 0.13 μm SiGe Technology," *IEEE J. Solid-State Circuits*, vol. 49, no. 9, pp.

1905-1915, Sept. 2014.

[10]   B. H. Ku et al., "A 77–81-GHz 16-Element Phased-Array Receiver With $\pm 50^{\circ}$ Beam Scanning for Advanced Automotive Radars," *IEEE Trans. Microw. Theory Techn.*, vol. 62, no. 11, pp. 2823-2832, Nov. 2014.

[11]   T. Jaeschke, C. Bredendiek, S. Küppers and N. Pohl, "High-Precision D-Band FMCW-Radar Sensor Based on a Wideband SiGe-Transceiver MMIC," *IEEE Trans. Microw. Theory Techn.*, vol. 62, no. 12, pp. 3582-3597, Dec. 2014.

[12]   T. Mitomo, N. Ono, H. Hoshino, Y. Yoshihara, O. Watanabe and I. Seto, "A 77 GHz 90 nm CMOS Transceiver for FMCW Radar Applications," *IEEE J. Solid-State Circuits,* vol. 45, no. 4, pp. 928-937, April 2010.

[13]   J. Lee, Y. A. Li, M. H. Hung and S. J. Huang, "A Fully-Integrated 77-GHz FMCW Radar Transceiver in 65-nm CMOS Technology," *IEEE J. Solid-State Circuits,* vol. 45, no. 12, pp. 2746-2756, Dec. 2010.

[14]   C. Cui, S. K. Kim, R. Song, J. H. Song, S. Nam and B. S. Kim, "A 77-GHz FMCW Radar System Using On-Chip Waveguide Feeders in 65-nm CMOS," *IEEE Trans. Microw. Theory Techn.*, vol. 63, no. 11, pp. 3736-3746, Nov. 2015.

[15]   T.-N. Luo et al., "A 77-GHz CMOS FMCW Frequency Synthesizer with Reconfigurable Chirps," *IEEE Trans. Microw. Theory Techn.*, vol. 61, no. 7, pp. 2641-2647, July 2013.

[16]   L. Bin, "One-Coincidence Sequences with Specified Distance Between Adjacent Symbols for Frequency-Hopping Multiple Access," *IEEE Trans. Commun.*, vol. 45, no. 4, pp. 408-410, Apr 1997.

[17]   L. Wronski et al., "Extended Hyperbolic Congruential Frequency Hop Code: Generation and Bounds for Cross- and Auto-Ambiguity Function," *IEEE Trans. Commun.*, vol. 44, no. 3, pp. 301-305, Mar 1996.

[18]   V. Giannini et al., "A 79 GHz Phase-Modulated 4 GHz-BW CW Radar Transmitter in 28 nm CMOS," *IEEE J. Solid-State Circuits,* vol. 49, no. 12, pp. 2925-2937, Dec 2014.

[19]   Robert M. O'Donnell, courtesy of IEEE New Hampshire Section Guest Lecturer, Jan 2011.